Chapter 2

Measurement of Aircraft State and Thermodynamic and Dynamic Variables

Jens Bange, Marco Esposito, Donald H. Lenschow, Philip R. A. Brown, Volker Dreiling, Andreas Giez, Larry Mahrt, Szymon P. Malinowski, Alfred R. Rodi, Raymond A. Shaw, Holger Siebert, Herman Smit, and Martin Zöger

2.1 Introduction

Insofar as the atmosphere is part of a giant heat engine, the most fundamental variables that must be quantified are those describing its thermodynamic state and the air motions (wind). Therefore, this chapter focuses on describing methods for measuring basic thermodynamic and dynamic variables of the atmosphere, including aspects and calibration strategies that are unique to performing such measurements from airborne platforms. However, in order to be able to analyze airborne thermodynamic and dynamic measurements, aircraft motion and attitude have to be measured as well, both for the purpose of placing measurements in an Earth coordinate system and for making corrections that depend on those factors. Therefore, this chapter starts by describing techniques to measure these aircraft state parameters.

The chapter begins with some historical context (Section 2.2), immediately followed by a description of methods for measuring the motion, position, and attitude of the airborne measurement platform itself (Section 2.3). The structure of the remainder of the chapter is organized with the following train of logic: scalar properties of the atmosphere are dealt with first, followed by vector properties, and finally, the two properties are combined in the discussion of flux measurements. The scalar properties that are of primary relevance to the thermodynamic state of the atmosphere are static air pressure (Section 2.4), atmospheric temperature (Section 2.5), and water vapor (Section 2.6). Water vapor is one of several trace gases of atmospheric relevance, but it is particularly highlighted here because of its profoundly important coupling to the atmospheric thermodynamic state (e.g., through latent heating/cooling and through infrared (IR) absorption) and the fact that water is common in the atmosphere in all three phases (gaseous, liquid, and solid, i.e., ice), with respective phase transitions. Water vapor by itself could be the subject of its own chapter, but we have chosen to keep it in the context of the other thermodynamic and dynamic variables, for example, temperature, that combine to give critical thermodynamic variables such as relative humidity and supersaturation. The treatment of the dynamic motions of the atmosphere is divided into measurement of the large-scale, three-dimensional wind vector (Section 2.7) and the measurement of smaller-scale turbulent motions (Section 2.8). The chapter culminates with a treatment of flux measurements (Section 2.9), which ultimately are responsible for the changing state of the atmosphere itself.

2.2 Historical

The history of airborne measurements for atmospheric research can be traced back to free air balloon sounding of the atmosphere. The first meteorological ascent was reported by the French physicist, Jacques Charles, on 1 December 1783 in a hydrogen balloon equipped with a barometer and a thermometer. He recorded a decrease in temperature with height and estimated the atmospheric lapse rate. Joseph Louis Gay-Lussac and Jean-Baptiste Biot made a hot-air balloon ascent in 1804 to a height of 6.4 km in an early investigation of the Earth's atmosphere and measured temperature and moisture

at different heights. They reported that the composition of the atmosphere does not change with decreasing pressure (increasing altitude). Manned balloons continued to be used throughout the next couple of centuries with the obvious advantage of being able to follow an air mass and thus allowing very detailed measurements in a small volume of air, but with the disadvantage of limited sampling statistics. In the early 1930s, Heinz Lettau and Werner Schwerdtfeger made direct measurements of vertical wind velocity in the lowest 4 km of the troposphere from a balloon using a combination of a rate-of-climb meter to keep the balloon height constant and a sensitive anemometer to measure the vertical air velocity relative to the balloon. They estimated that the accuracy of their technique was better than 0.2 m s^{-1} (Lewis, 1997).

The use of powered aircraft for airborne measurements of atmospheric parameters goes back to at least 1911 when in Germany, Richard Assmann, the inventor of the aspirated psychrometer, motivated the aircraft designer, August Euler, to modify one of his aircraft to make upper-air soundings. The following year a meteorograph was installed in an Euler monoplane and it recorded pressure and temperature up to 1100 m altitude. Aircraft continued to be used for temperature soundings, in some cases on a daily basis, from the 1920s through the World War II. These measurements played a role in the major advances that occurred in synoptic meteorology during these years. Eventually, their routine sounding role diminished as pilot balloons and radiosondes became the standard tools for atmospheric sounding.

Thermodynamic and turbulence measurements were performed in 1936 with a Potez 540 aircraft from the French Air Force in the Puy de Sancy Mountain area (Dupont, 1938). The aircraft was equipped with an "anémoclinomètre" for the airspeed and attack and drift angles measurements, an accelerometer with three piezoelectrical channels for the vertical acceleration component, and a "météograph" for the pressure, temperature, and hygrometry measurements. Several flights were performed over the National Glider School Center to characterize turbulence and dynamic properties over the mountain site.

The use of aircraft for intensive research programs continued to expand. For example, a series of temperature and humidity soundings from aircraft in the lowest 300 m over the ocean in the fall of 1944 was used to study modification of stably stratified air along its trajectory as it passed from land to a relatively cold ocean offshore of Massachusetts, USA (Craig, 1949).

Turbulence measurements from aircraft date back to at least the early 1950s when a US Navy PBY-6A instrumented with a vertical accelerometer was used by Joanne Malkus and Andrew Bunker to estimate a "turbulence index" for cloud dynamics observations (Malkus, 1954). Later, an anemometer was combined with the vertical acceleration measurements to estimate vertical and longitudinal air velocity fluctuations, and thus to calculate vertical momentum flux (Bunker, 1955).

In the mid-1950s, a more complete turbulence measuring system was used on a McDonnell FH-1 (the first all-jet aircraft) to measure vertical velocity spectra in the planetary boundary layer. This system used either a rotating vane or a differential pressure probe mounted on a nose boom to measure the aircraft attack angle, an integrating accelerometer to measure aircraft velocity fluctuations relative to the Earth, and an integrating rate gyroscope to measure pitch angle fluctuations. By combining these measurements, fluctuations of vertical wind velocity were estimated (Lappe and Davidson, 1963).

A different approach to measuring turbulence intensity was used by MacCready (1964) starting in the early 1960s, who disregarded the long wavelength contributions to the longitudinal air velocity fluctuations by band-pass filtering the output of an airspeed sensor to estimate the turbulence dissipation from the Kolmogorov hypothesis. This provided a simple easily implemented system to provide a standardized measure of turbulence, albeit over a limited wavelength region, as well as a measure of the total turbulence energy production by equating it to the turbulence dissipation.

The next step in improving the complexity and accuracy for vertical wind velocity measurements was taken in the early 1960s in Australia, with the development of a system on a Douglas DC-3 by Telford and Warner (1962). They combined a nose-boom-mounted vane with a free gyroscope and a vertically stabilized (using signals from the free gyroscope) accelerometer. This reduced errors present in previous systems due to the varying contribution of gravity to the measured acceleration resulting from attitude angle variations. They also incorporated a fast temperature sensor and wet-bulb thermometer to measure heat and water vapor fluxes.

Afterward, an inertial navigation system (INS) was integrated, with improved accuracy and reduced drift rates, to measure the translational and rotational aircraft motions, as well as the absolute location of the aircraft. Today, GPS-based instruments are also utilized in combination with Inertial Measuring Units (IMUs) to provide a lighter and less expensive alternative to INS. In contrast, the air motion sensing systems have changed little in the past few decades and are now the limiting factor in measuring air motion.

At present, there is a remarkable variety of instrumented airborne platforms for atmospheric and environmental measurements, including high-performance jet aircraft for high-altitude and long-range measurements, smaller turboprop aircraft for intensive boundary layer measurements, armored aircraft for thunderstorm penetration, slow-moving helicopter-towed platforms for high-resolution measurements, and an emerging fleet of relatively small, remotely piloted vehicles carrying miniaturized but still highly capable instrument packages. Indeed, the airborne platforms are as varied and innovative as the instruments they carry, all matched to the specialized research objectives that drive the continuing innovation.

2.3 Aircraft State Variables

In order to place measurements into a proper geographical reference frame it is necessary to precisely measure the position and attitude of the aircraft from which measurements are made. These variables, including aircraft height or altitude, attitude (e.g., yaw, pitch, roll angles), position, and velocity, are collectively defined as the aircraft state.

2.3.1 Barometric Measurement of Aircraft Height

Hypsometric (or pressure) altitude can be estimated by an integration of the hydrostatic equation using measurements of virtual temperature T_{vir} and static air pressure p, assuming that the sounding is invariant as follows:

$$z - z_0 = -\int_{p_0}^{p} \frac{R_{dry} \cdot T_{vir}}{g} \, d\ln p \tag{2.1}$$

where $R_{dry} = 287.05\ J\ kg^{-1}\ K^{-1}$ is the specific gas constant of dry air. The gravitational acceleration g varies with height z and location (geographic latitude). Errors result from horizontal temperature gradients, and also when nonhydrostatic conditions exist, for example, in strong atmospheric motions. Further errors are introduced when neglecting the effect of humidity and vertical variation of the gravitational acceleration g.

Alternatively, standard atmosphere models can be used to estimate the temperature from the pressure, which can then be integrated to obtain pressure altitude. The International Standard Atmosphere (ISA) sets the international standard (ISO, 1975). Below 30 km altitude, the ISA model is identical to that of the International Civil Aviation Organization (ICAO) and the US Standard Atmosphere, with variables as shown in Table 2.1. These standard atmospheres assume dry atmospheric conditions.

Table 2.1 ISA Standard Atmosphere Properties (base values) in the Troposphere and Stratosphere

Layer	Geopotential height h_0 (gpkm)	Geometric height z_0 (km)	Lapse Rate γ_0 (°C gpkm^{-1})	Temperature T_0 (°C)	Pressure p_0 (Pa)
0	0	0.0	−6.5	+15.0	101 325
1	11	11.019	+0.0	−56.5	22 632
2	20	20.063	+1.0	−56.5	5 474.9
3	32	32.162	+2.8	−44.5	868.02

Variation in the value of gravitational acceleration g is small. To account for this, instead of the geometric altitude, atmospheric models use geopotential height measured in geopotential meters (gpm), defined as

$$h - h_0 = \frac{1}{g_n}\int_{z_0}^{z} g(z')\,dz' = -R_{dry} \cdot \int_{p_0}^{p} T_{vir}\, d\ln p \tag{2.2}$$

where the subscript 0 refers to a reference state for each atmospheric layer as defined in Table 2.1, and $g_n = 9.80665$. After integration for each layer with constant lapse rate γ_0 (also given in Table 2.1), it can be shown that

$$p = p_0 \cdot \left(1 - \frac{\gamma_0 \cdot h}{T_0}\right)^{g_n/(R_{dry} \cdot \gamma_0)} \quad \textbf{2.3}$$

and

$$h = h_0 + \frac{T_0}{\gamma} \cdot \left[1 - \left(\frac{p}{p_0}\right)^{R_{dry} \cdot \gamma_0 / g_n}\right] \quad \textbf{2.4}$$

see Iribarne and Godson (1981). For the dry, tropospheric layer, using the ISA constants, we obtain

$$h = 44\,331 \cdot \left[1 - \left(\frac{p}{p_0}\right)^{0.19026}\right] \quad 2.5$$

where h is obtained in gpm. In Eq. (2.5), p_0 is 1013.25 hPa, corresponding to the lowest atmospheric layer in the ISA (Table 2.1). An aircraft pressure altimeter in this lowest atmospheric layer indicates the ISA altitude when the altimeter setting is 1013.25 hPa. Typically, the altimeter setting is adjusted so that the altimeter reads exactly the airport altitude on landing. The details of how altimeter setting is mechanized in an aircraft pressure altimeter can be found in Iribarne and Godson (1981).

Both the hypsometric altitude from Eq. (2.1) and the pressure altitude from Eq. (2.5) assume that there are no horizontal pressure gradients. Height measurements based on RADAR are not covered here. The sum of RADAR altitude plus the height of the terrain above sea level approximates hypsometric or pressure altitude measurements, but accurate terrain data is not available at very fine scale, and surface artifacts such as buildings can complicate that determination except, of course, over the sea. Neither of these altitude estimates is as inherently accurate as those from the Global Navigation Satellite System, as described in Section 2.3.3. For use in comparing airborne measurements with atmospheric model output, pressure or potential temperature could be less ambiguous measures of height.

2.3.2 Inertial Attitude, Velocity, and Position

2.3.2.1 System Concepts

IMUs using Newton's laws, applied to motion on a rotating planet, integrate a triad of linear accelerations to determine aircraft velocity and position. Detailed theory of operation and design criteria for navigation units based on IMUs are presented in the studies by Broxmeyer (1964) and O'Donnell (1964). The accelerometer orientation must be known to accommodate accelerations due to gravity, and this is accomplished by mounting on a stable platform.

Two main approaches are in general use: gimballed and strapdown systems. The gimballed system is typically mechanized to keep the stabilized platform containing the accelerometers level with respect to the Earths gravity, rotating as necessary to maintain verticality as the aircraft moves, incorporating the effect of changes in the gravity vector as the aircraft changes latitude and altitude. The gimbals are a set of three rings that let the platform keep the same orientation while the vehicle rotates around it. Attitude angles can then be measured directly from the gimbal orientation. The big disadvantage of this approach is the relatively high cost and mechanical complexity causing reliability challenges related to the many precision mechanical parts. The coordinate transformation between Earth-fixed and aircraft body axis systems is described by Axford (1968) and Lenschow (1972). Figure 2.1 (Axford, 1968) shows the arrangement of a gimballed system and defines the coordinate transformation variables for its use.

Figure 2.1 Sketch of gimbal system. (Source: Redrawn from Axford (1968). Copyright 1968 American Meteorological Society. Reprinted with permission.)

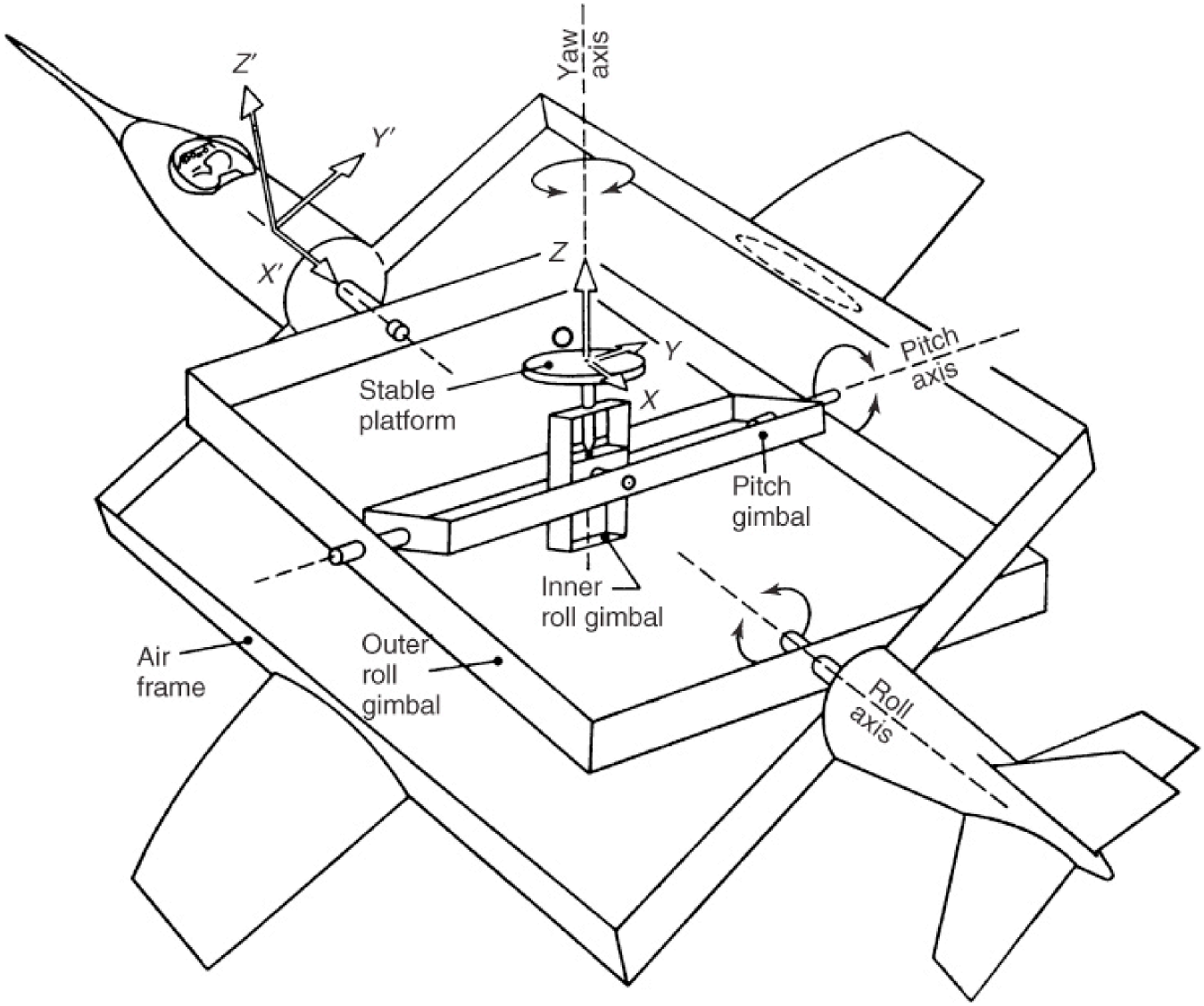

In strapdown systems, which comprise most of the IMUs used in atmospheric research at present, accelerometers are fixed to the aircraft, and linear and angular acceleration measurements are integrated using a model to continually compute the orientation of gravity to the vehicle axis, creating a virtual stabilized platform. Compared to the gimballed systems, strapdown systems offer lower cost and higher reliability but require higher maximum angular rate capability and higher sampling rate capability to sufficiently capture aircraft motion on a maneuvering aircraft (Barbour, 2010). IMUs integrated into an INS with a gyroscope error of 0.01° h^{-1} will result in a navigation error of ~2 km h^{-1} of operation.

2.3.2.2 Attitude Angle Definitions

Standard definitions for the attitude angles and other motion variables can be found in ISO 1151-1 (ISO, 1985) and ISO 1151-2 (ISO, 1988). A conventional INS defines the Earth-based coordinate system to be north-east-down (NED) and the aircraft body axis system to be forward-right-down (*XYZ*). The transformation matrix from the body axis *XYZ* to the Earth-based NED system has three successive rotations that are prescribed by the order of the gimbals (roll innermost). For strapdown systems, the equations are written to emulate this gimbal order that defines the attitude angles using the Tait-Bryan sequence of rotations: (i) rotate to wings horizontal around body *X* (forward)-axis by roll angle (ϕ, right wing down positive); (ii) rotate to *X*-axis horizontal about body *Y* (right)-axis by pitch angle (θ, nose up positive); and (iii) rotate about *Z* (down)-axis to north by heading (ψ, true heading, positive from north toward east). Transforming a vector in the *XYZ* body axis to Earth-based NED coordinates requires the roll **R**, pitch **P**, and heading **H** rotation matrices

$$\begin{aligned}
\mathbf{H} &= \begin{pmatrix} \cos\psi & -\sin\psi & 0 \\ \sin\psi & \cos\psi & 0 \\ 0 & 0 & 1 \end{pmatrix}, \\
\mathbf{P} &= \begin{pmatrix} \cos\theta & 0 & \sin\theta \\ 0 & 1 & 0 \\ -\sin\theta & 0 & \cos\theta \end{pmatrix}, \\
\mathbf{R} &= \begin{pmatrix} 1 & 0 & 0 \\ 0 & \cos\phi & -\sin\phi \\ 0 & \sin\phi & \cos\phi \end{pmatrix}
\end{aligned} \tag{2.6}$$

to be applied to the vector in the following order:

$$\begin{aligned}
\mathbf{T}_N^B &= \mathbf{H}\,(\mathbf{P}\,\mathbf{R}), \\
\begin{pmatrix} N \\ E \\ D \end{pmatrix} &= \mathbf{T}_N^B \begin{pmatrix} X \\ Y \\ Z \end{pmatrix}
\end{aligned} \tag{2.7}$$

2.3.2.3 Gyroscopes and Accelerometers

Doebelin (1990) presents an overview of linear accelerometers and 3D gyroscopic angular displacement and angular velocity (rate) sensors. Barbour (2010) and Schmidt and Phillips (2010); Schmidt (2010) survey current inertial sensor issues and trends. Spinning electrically suspended gyroscopes (ESGs) offer the highest accuracy and stability, with the rotor supported in vacuum by an electric field, thus nearly eliminating errors caused by friction. Currently, there is an upsurge in solid-state sensors that include microelectromechanical systems (MEMS) devices, ring laser gyros (RLGs), fiber-optic gyros (FOGs), and interferometric gyros (IFOGs), which have significant cost, size, and weight advantages over spinning devices. Accelerometers are pendulous servo accelerometers, resonant vibrating beam accelerometers (VBAs), or MEMS implementations of either of these.

Table 2.2 indicates the gyro bias and accelerometer bias requirements of each class of application. In an unaided INS, initial alignment must be accomplished carefully so that the initial tilt of the system does not put a component of gravity into the horizontal accelerometers. Alignment is accomplished by tilting to zero the horizontal acceleration to establish level, and the initial heading is accomplished by establishing north by alignment with the Earth's rotation rate ($0.002\ ^\circ\ s^{-1}$).

Table 2.2 Performance of Classes of Unaided INS

Class	Position performance	Gyro technology	Accelerometer technology	Gyro bias	Acceleration bias
Military grade	1 nmi $(24\,h)^{-1}$	ESG, RLG FOG	Servo Accelerometer	$<0.005^{\circ}\,(h^{-1})$	30 mg
Navigation grade	1 nmi h^{-1}	RLG FOG	Servo Accelerometer Vibrating Beam	$0.01^{\circ}\,(h^{-1})$	50 mg
Tactical grade	>10 nmi h^{-1}	RLG FOG	Servo Accelerometer Vibrating beam MEMS	$1^{\circ}\,(h^{-1})$	1 mg
AHRS		MEMS, RLG FOG, Coriolis	MEMS	$1–10^{\circ}\,(h^{-1})$	1 mg
Control system		Coriolis	MEMS	$10–1000^{\circ}\,(h^{-1})$	10 mg

Table 2.3 shows the expected uncertainties from unaided navigation-grade INS.

Table 2.3 Accuracy of Unaided Navigation-Grade INS (Honeywell LaserRef2 SM after 6 h).

Variable	Accuracy
Position	1.5 km h^{-1}
Ground velocity	4.10 m s^{-1}
Vertical velocity	0.15 m s^{-1} (baro-damped)
Pitch and roll angles	0.05°
True heading	0.2°

Source: From Honeywell (1988).

2.3.2.4 Inertial-Barometric Corrections

Unaided INS does not have sufficient information available to damp errors in the Earth-vertical coordinate. Barometric pressure can be used to limit errors in the vertical acceleration that cause unbounded drift. A third-order baro-inertial loop described by Blanchard (1971) can be used for this. Lenschow (1986) discusses the considerations for choosing the time constant for the mechanization of the loop, being a trade-off among minimizing the effect of high-frequency noise in the pressure measurement, minimizing the recovery time from errors, and improving long-term stability. A time constant of 60 s has been used for the National Center for Atmospheric Research (NCAR) aircraft.

2.3.3 Satellite Navigation by Global Navigation Satellite Systems

Global Navigation Satellite Systems (GNSS) are constellations of satellites in medium Earth orbit at heights of about 2.5×10^7 m, corresponding to an orbital period of roughly 12 s. Gleason and Gebre-Egziabher (2009) provide detailed information about GNSS methodology and expected errors. Table 2.4 lists the status of GNSS as of 2010. Receivers compatible with multiple constellations benefit from the larger number of satellites in view.

Table 2.4 Overview of Operational and Planned Global Navigation Satellite Systems

System	Country	Number of satellites	Frequencies	Status
GPS	USA	24	1.57542 GHz (L1 signal) 1.2276 GHz (L2 signal)	Operational
GLONASS[a]	Russia	21	Around 1.602 GHz (SP) Around 1.246 GHz (SP)	Operational, six satellites in maintenance
Galileo[b]	EU	30	1.164–1.215 GHz (E5a and E5b) 1.215–1.300 GHz (E6) 1.559–1.592 GHz (E2–L1–E11)	Operational in 2014
COMPASS[c]	China	30	B1: 1.561098 GHz B1–2: 1.589742 GHz B2: 1.20714 GHz B3: 1.26852 GHz	Operational in 2015

[a]GLONASS stems from the Russian words Globalnaja Navigaziona Systema, which means in English, the Global Navigation System.
[b]Galileo is not an acronym, the system is named after the famous Italian astronomer Galileo Galilei (1564–1642).
[c]COMPASS means BeiDou (Compass) Navigation Satellite System. Compass is the translation from Chinese

Each satellite vehicle (SV) broadcasts a precise time measurement along with its ephemeris. GPS receivers use this to determine the transit time of the signal, which is then converted to distance (called *pseudorange*). Satellite positions can be obtained from either the broadcast ephemeris or the more accurate ephemeris published within hours or days, which can be incorporated into postprocessing of the GNSS signals. Four (or more) pseudorange measurements are used to unambiguously compute the receiver position using triangulation. Adding more SV signals increases the accuracy of the position estimate.

2.3.3.1 GNSS Signals

The details of the coding and decoding of GNSS signals are discussed in the texts of Gleason and Gebre-Egziabher (2009); Bevly and Cobb (2010); Hofmann-Wellenhof, Lichtenegger, and Collins (2001). The US GPS provides two precision positioning signals (military-accessible P-code) on frequencies L1 (1575.42 MHz) and L2 (1227.6 MHz) and a clear acquisition signal (C/A code) on L1. A third frequency L5 (1176.5 MHz) was added in 2009. Selective availability (SA) – the intentional addition of time varying errors of up to 100 m (328 ft) to the publicly available navigation signals – was discontinued in 2001.

In addition to the pseudorange-only triangulation techniques, carrier phase (CP) tracking on multiple frequencies can produce centimeter accuracies. CP techniques were developed for precise surveying and geodesy (including surface motions presaging earthquakes, continental drift), but they have also been recently successfully applied to moving vehicles such as aircraft. Each cycle of the L1 and L2 carrier frequency is about 19 cm long, and phase can be measured to better than 1% so that millimeter accuracy can be obtained under optimal conditions.

2.3.3.2 Differential GNSS

Differential GNSS (DGNSS), commonly termed *differential GPS* (*DGPS*), is a means of removing almost all navigation errors (discussed later). GNSS receivers are installed at strategically placed ground locations. Several networks of these ground stations exist. Using the precisely known location of the ground-based stations, the simultaneous measurements of the SV location can be used to solve for satellite clock and ephemeris errors, and ionosphere and troposphere delays (see below). When reference stations are closely located, errors are highly correlated, and this assumption is used to solve the navigation equations simultaneously to estimate the errors in the moving platform. Also, wide area corrections can be made by estimating corrections over an extended area. Oceanic areas void of stations are an obstacle to these approaches.

2.3.3.3 Position Errors and Accuracy of Satellite Navigation

The true location of the satellite is known very accurately because the orbits of the GPS satellites are precisely determined by continuous error checking and computation. The broadcast ephemerides have 1–2 m accuracy; however, postprocessing centers provide ±15 cm (available every 2 h), ±5 cm (next day), and ± 2 cm (about two weeks) accuracies.

The speed of the GPS signals varies as they pass through the Earth's atmosphere, with the ionosphere having the largest effect. Consequently, the errors become greater for longer paths through the atmosphere, and the geometry of the triangulation of the receiver location then needs to be considered in estimating errors.

Ionospheric delay (dispersion) effects depend on the total electron content (TEC) in the path at altitudes of 50–100 km and can be very large. Ionospheric models, such as the one by Klobuchar (1996), can provide useful estimates of the effect. Measurement of delays for two or more frequency bands (L1 and L2 CP for the GPS) allows a more precise correction, and under optimal conditions, "ionosphere-free" solutions can be obtained.

Propagation errors caused by refractivity variations in the troposphere, which result primarily from variations in temperature and water vapor mixing ratio, are smaller than those caused by the ionosphere. Atmospheric models can be used here also.

GPS signals can reflect from external reflectors near the receiver antenna, and mixing the direct and reflected signals distorts the received signal tracking. Multipath effects are much less severe in aircraft at altitudes above reflecting surfaces, but low-level flights near buildings and/or topography can result in errors. For very precise positioning, these effects can be mitigated or eliminated using DGPS.

When visible GPS satellites are close together in the sky (i.e., small angular separation), the navigation solution becomes less precise. A figure of merit termed *dilution of precision* (*DOP*) provides a measure of how errors propagate through the geometry of multiple satellite position determination from the pseudorange measurements. The components of DOP-HDOP, VDOP, PDOP, and TDOP give horizontal, vertical, 3D position, and time dilutions, respectively. Hofmann-Wellenhof, Lichtenegger, and Collins (2001) provide a complete description of the DOP determination. DOP values of 1 are optimal, with increasing DOPs indicating increasing degradation of the solution, while DOPs of 6 are considered unacceptable.

2.3.4 Integrated IMU/GNSS Systems for Position and Attitude Determination

INS systems with GNSS aiding to minimize errors have been available since the 1970s. Recent advances in the GNSS technology and real-time and postprocessing software have provided combined systems with smaller than 1 m real-time error. Kalman filtering is widely used to merge the continuous IMU sensor data with the intermittent GNSS data (Brown and Hwang, 1997). Multiple GNSS antenna configurations are available that increase the accuracy of heading, but the three-antenna configuration can also be used to solve for the three attitude angles. DGPS error correction is available in real-time through terrestrial or satellite-based communication to the aircraft.

The biggest issue with the integrated IMU/GNSS systems is performance during periods of GNSS denial, that is, when satellite coverage is poor or unavailable, or when the number of satellites in view drops, as frequently occurs during aircraft maneuvers resulting in very poor DOP. Tactical-grade IMU technology has been shown to provide adequate stability during those periods.

2.3.5 Summary, Gaps, Emerging Technologies

In just a short period, the integrated IMU/GNSS technology has bridged the gap between relatively inaccurate navigation aids and expensive navigation-grade INS, providing small low-cost systems for attitude, position, and velocity determination. The anticipation is that this trend will continue with advances in FOG and MEMS gyroscope technology to reduce size and cost even further. The addition of the Galileo and the COMPASS constellations will bring further advantages in terms of the number of satellites in view. Additional frequencies on the GNSS are coming online, which will allow further reduction of GNSS propagation errors to make 1 cm accuracy routine on a maneuvering aircraft.

2.4 Static Air Pressure

A knowledge of static air pressure is critical for a wide range of atmospheric applications. It is needed to understand atmospheric measurements onboard an aircraft, it is used as a vertical coordinate, and it is an important parameter for physical and chemical atmospheric processes. Measurements of static air pressure onboard an aircraft also provide information on the actual flight altitude. This parameter influences the calculation of aircraft speed and other performance data as well as the cabin pressure regulation. Historically, with the increasing speed of aircraft, distortion of flow by the fuselage became more important. In the 1950s, Gracey (1956) published a fundamental work dealing with the shape of fuselage, shape of probes, and influence of speed on the measurement of static air pressure at various positions on aircraft. Today, we use models to calculate air stream around arbitrarily shaped bodies, but the results of this paper still give profound insight into this subject.

The concepts of measuring static air pressure have not changed much since then. Along the fuselage, a number of positions can be found where static pressure is found to be close to $p_{s\infty}$, the undisturbed static air pressure at the same altitude. Virtually, all the positions show cross-sensitivity to maneuvers. So tools such as booms in different positions are used to shift static air pressure probes out of the influence of the aircraft.

Instead of static air pressure, generally, some expression of flight altitude is given in avionic data sets. But the most useful coordinate for vertical position within the atmosphere is static air pressure, which is an expression for the weight of the atmosphere above the actual flight level. This is expressed by the hydrostatic equation.

$$\frac{\mathrm{d}p}{\mathrm{d}z} = -g \cdot \rho \tag{2.8}$$

where p is the air pressure (in units of Pa) at a given altitude z (given in units of m), g is the acceleration due to Earth gravity (gravitational acceleration) in units of m s^{-2}, and ρ is the density of air (in kg m^{-3}). Using the relation for an ideal gas,

$$\frac{p}{\rho} = R_{\mathrm{dry}} \cdot T \tag{2.9}$$

where R_{dry} = 287.05 J kg^{-1} K^{-1} is the individual gas constant for (dry) air and T is the air temperature in Kelvin, we have the differential form of the hydrostatic equation:

$$\frac{\mathrm{d}p}{p} = -\frac{g}{R_{\mathrm{dry}}} \cdot \frac{\mathrm{d}z}{T} \tag{2.10}$$

For a given local position, air pressure is steadily decreasing for growing altitude z. Although air temperature is decreasing with a gradient of – 0.0065 K m^{-1} as a global mean for tropospheric standard day conditions, the local deviation may be large. To express the air temperature for a given atmospheric layer $\Delta z = z_2 - z_1$, the mean temperature $\overline{T}$ is defined by

$$\overline{T} = \Delta z \cdot \left(\int_{z_1}^{z_2} \frac{\mathrm{d}z}{T} \right)^{-1} \tag{2.11}$$

Equation (2.11) can be applied to humid air by replacing the air temperature T with the virtual temperature T_{vir}. At this point, a problem arises that is typical for aviation: we can measure all atmospheric parameters *in situ*, but we also need to

know the temperature (and humidity) profile below the aircraft, which normally is not known. This limits the practical application of Eq. (2.10) or enforces assumptions on the vertical temperature distribution. The density effect of humidity, which is accounted for by the virtual temperature, plays a major role at lower flight altitudes, whereas the low temperatures of the upper troposphere allow only relatively low water vapor pressures and hence small density effects.

This uncertainty is a very important problem in aviation, so a fundamental solution had to be found. This was done by defining an atmospheric standard. Since 1976, the last revision of the US Standard Atmosphere, the standard is based on a mean sea level temperature of 288.15 K, in which the pressure at mean sea level for a "standard day" is set to 101 325 Pa. The vertical temperature gradient for troposphere is set to a mean value of $-0.0065\ \mathrm{K\ m^{-1}}$. At the mean altitude of the tropopause (defined as 11 000 m) and above, up to an altitude of 20 000 m, the temperature is set constant at 231.65 K. This is the atmospheric layer important for normal aviation, although the tabulated standards continue further up to 86 000 m.

Applying this temperature distribution, we can calculate the altitude for a standard day from a pressure measurement alone in any given flight level. In aviation, this is exactly what happened to the avionic instrument standards. An altimeter that is set to standard conditions assumes a sea level pressure of 101 325 Pa and a temperature change according to $-0.0065\ \mathrm{K\ m^{-1}}$. Then, the instrument shows the pressure altitude. The importance of this standard procedure in aviation is the reliable vertical separation of traffic in the air. Safety assessment requests a classification of the measurement to a defined accuracy.

On the other hand, the given pressure altitude may deviate hundreds of meters from geometric altitude, which is nowadays easily reported from satellite-based measurements or calculated from independent atmospheric profile data. Also, the standard setting cannot be used in the vicinity of ground-based obstacles. There is a different procedure for low altitudes, where "low" depends on regional topography as well. In case of low flight altitudes (e.g., takeoff and landing), the real ground pressure will be set as a reference. Then, the instrument shows barometric altitude, where the actual measured ground pressure (e.g., taken at an airport tower at the actual field height) is extrapolated down to sea level for a reference.

2.4.1 Position Error

The air pressure p is approximated by the static air pressure indicated by p_s in the following discussion. p_s is the measured pressure corrected for the static defect so it is the best estimate of p. Methods for reliable measurement of static air pressure on fast-moving platforms are discussed in this section, with specific attention to the dependence of pressure measurements on their position on the aircraft; these deviations from background static air pressure are denoted as position errors. Sensor elements and conditioners are not discussed in detail. As far as these parts are mounted in unpressurized bays with widely changing environmental conditions, it is at least important to make sure that the instrument's signal processing is insensitive to extreme temperatures and pressures. All pressure sensors show more or less strong sensitivity to temperature changes, which, for best results, can be treated by stabilizing the sensors' temperature within a narrow interval. Pressure measurements often use some length of tubing, so it is necessary to care for the total volume involved and to keep in mind that the pressure signal can be damped and delayed. Neglecting measurement errors produced by tubing and sensor elements for now, the error of the static air pressure p_s is mainly the position error Δp_s, as defined in more detail in the next paragraph.

The fuselage of an aircraft distorts the flow field in a typical way, and the local pressure at the surface of the fuselage may deviate by some 1000 Pa from $p_{s\infty}$, the undisturbed static air pressure. Figure 2.2 (Haering, 1995) shows complex structures of positive and negative deviations from undisturbed $p_{s\infty}$, but moreover, these patterns of pressure deviation will vary with maneuvers such as turns, low or high speeds, and aircraft weight. This will result in errors for static air pressure that depend on the measurement location, called *position errors*.

Figure 2.2 Pressure deviation around fuselage. (Source: Adapted from Haering (1995). Reprinted with permission. Courtesy of Tom Anderson.)

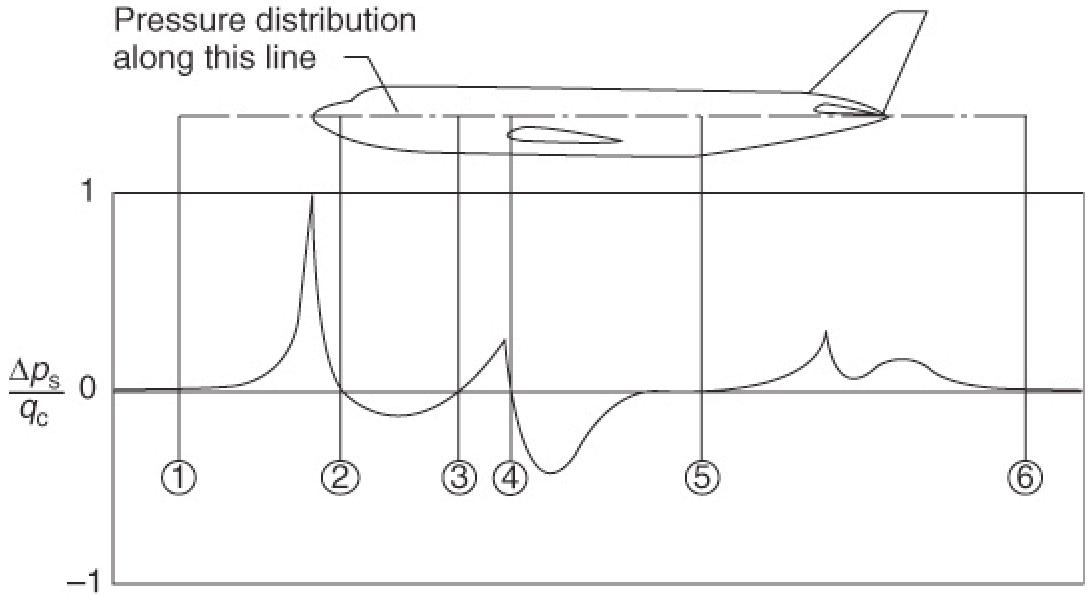

For a standard aircraft, a number of different orifices along both sides of the fuselage are combined to provide a mean value over a number of sensors, which serve as an important reference. The positions of the orifices are carefully selected for each aircraft model : by modeling and testing, a manufacturer defines those locations where pressure deformation is close to zero. This holds usually for a "clean" aircraft, that is, without further devices mounted outside the fuselage or wings. Any change in the outer shape has the capability to change the quality of a pressure port.

Errors in static air pressure measurement also influence the measurement of the aircraft speed taken from a measurement of dynamic pressure q_c, which is the result of a difference of two large numbers:

2.12 $$q_c = p_t - p_{s\infty}$$

where p_t means total pressure, measured as the ram pressure of a pitot tube. An error in static air pressure will also produce an error in dynamic pressure and a correction will lead to a term of correction for speed. Although q_c can be measured directly as differential pressure between the two ports, the error can be expressed as a correcting term for the indicated static air pressure p_i.

2.13 $$\Delta p_s = p_{s\infty} - p_i$$

which leads to

2.14 $$q_c = p_t - (p_i + \Delta p_s)$$

The ram pressure p_t for speed reference is measured in a definite position in the nose area using a pitot tube, and as mentioned, the static air pressure can be measured through distributed orifices along the fuselage. It is also possible to use special tools such as a nose boom to put a flow sensor as far as possible out of the disturbed neighborhood of the fuselage.

The widely used five-hole probe (FHP) mounted at the tip of a boom reaches out into undisturbed flow fields and has better results for both dynamic ram pressure and static pressure. In addition, differential pressure measurements allow for determination of flow angles along vertical and cross axes. The blunt-tipped FHP for subsonic aircraft is a hemisphere on a cylindrical shaft. It combines a pitot port at the tip with a number of static bore holes around the shaft at a distance of about 4 shaft diameters behind the tip. Within the hemisphere, two pairs of ports for vertical (α, angle of attack) and crosswise (β, angle of sideslip) deviation from axial flow are positioned 45° off the axes for heading. The q_c signal shows some sensitivity to nonaxial flow, hitting the FHP with angles of more than 6° (de Leo and Hagen, 1976).

Some distance ahead of the nose, the influence of the fuselage on the pressure field may be very low, but still there is an effect on pressure generated by the boom itself. The deviation Δp_s at the boom tip is small but cannot be neglected. This is true for most other devices that may be used instead. An exception is the Flush Airdata Sensing (FADS) system that uses a system of many pressure ports distributed over the normal nose cap. This device needs no change in outer shape and hence produces no further influence on the pressure field. But for both versions, boom and FADS, adaptions

might be required to aircraft systems, such as RADAR. Both systems require further investigation of position errors by flight testing. Then, the most important question for test flights is to find a reliable measurement for $p_{s\infty}$, that is, a pressure sensor has to be put out into the undisturbed air.

2.4.1.1 Tower Flyby

Near the ground it is possible to use stationary ground-based pressure sensors to serve as reference. In a procedure called *tower flyby*, the pressure reference of the airport tower or other instruments can be used. Here it is necessary to know the exact altitude of the aircraft relative to the ground-based instrument. This can be achieved through (i) a known flight path, for example, the centerline of the runway; (ii) a flight altitude just high enough to avoid disturbance by ground effects; (iii) some optical device to get an independent measurement of the altitude (which, e.g., can be done by photography); or (iv) tracking of flight altitude by high-precision DGPS.

The procedure should include data taken on the runway by the aircraft system. In this case, the ground-based instrument has mainly to record the pressure changes during the flights. For highest accuracy, temperature and humidity will also be recorded. The altitude of the aircraft above the ground can be obtained from a photograph (e.g., by applying a self-scaling procedure using the length of the fuselage as a known constant to scale the distance between the aircraft and the runway). A sequence of tower flybys are carried out to cover the applicable range of speeds and attitudes (e.g., flap settings). The correction is simply given by Eq. (2.13), where $p_{s\infty}$ is calculated from Eq. (2.10).

2.4.1.2 Trailing Sonde

The characterization of airborne static air pressure measurements needs more combinations of speed and attitude than tower flyby can cover. Test flights have to be carried out at higher altitudes (higher speeds, lower density) as well. The independent measurement of $p_{s\infty}$ can then be delivered by a calibrated chase aircraft, flying in more or less close formation (but at least at the same flight level).

Without a chase aircraft, autonomous methods can be used to install calibration sensors on board of the tested aircraft. Means to eliminate the pressure deviation around the fuselage use probes put out to a distance under or behind the aircraft (the "trailing bomb" or the "trailing cone," respectively) connected by a long tube to the fuselage. Given that the sensors are positioned at distances where aircraft disturbances are minimal, the sensors read the undisturbed pressure directly. The method of the trailing bomb is more useful for slower aircraft or Mach numbers below about 0.5. The trailing cone probe works above Mach 0.3 and up into the supersonic speed range. This probe consists of a cone of resin with 35° opening angle and some circular openings, stabilizing the tubing against rotation. The cone produces drag that is needed to keep a long tube and a static air pressure probe lifted up behind the tail of the aircraft. In general, the turbulence field behind the aircraft moves downward. At the distance of about one to two wingspans, the probe should be free of turbulence. At high air speeds, the drag of the cone keeps the tubing and probe above the turbulent wake and the measurements are very close to $p_{s\infty}$.

Figure 2.3 shows that the correction of the indicated pressure, defined as

$$\frac{\Delta p_s}{q_c} = \frac{p_i - p_{tc}}{q_c} \tag{2.15}$$

where p_{tc} is the pressure reading of the trailing cone probe, approaches a constant value. It then remains almost constant in the speed range of Mach numbers between 0.35 and 0.75 and increases very strongly above. Furthermore, the correction clearly depends on the configuration of the aircraft (e.g., flap and gear positions). The data were taken at several flight levels and are valid only for a certain aircraft and for a defined configuration. With devices such as the FHP, it is also possible to investigate the dependence of Δp_s on the angles of attack, α, and sideslip, β. In this case, the error $\Delta p_{s\alpha\beta}$ of static air pressure can be expressed as a linear superposition:

$$\Delta p_{s\alpha\beta} = \Delta p_s + \Delta p_{s\alpha} + \Delta p_{s\beta} \tag{2.16}$$

which has been shown for a Falcon 20 by Boegel and Baumann (1991), analyzing a series of pitching or yawing oscillations.

Figure 2.3 Schematic correction of static pressure by trailing cone for a jet aircraft over a wide range of Mach numbers.

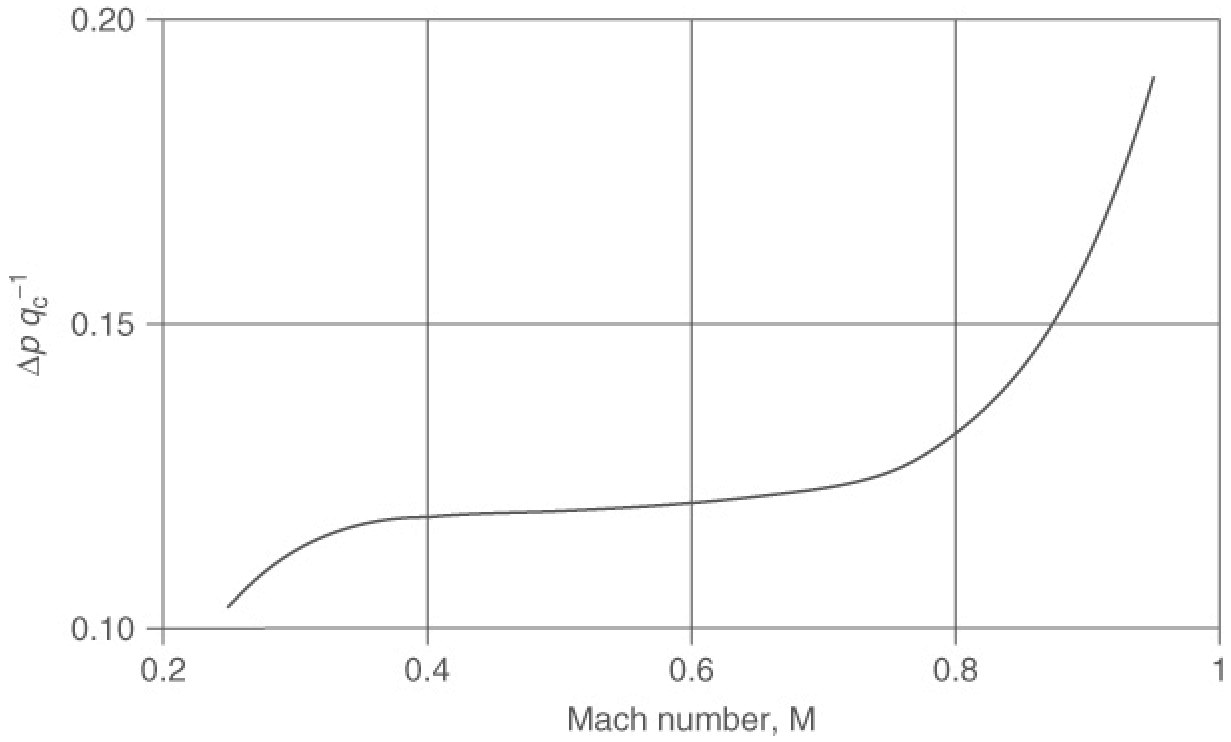

2.4.2 Summary

Static air pressure measurement onboard an aircraft depends on the configuration of the aircraft (flaps, landing gear, etc.), on the position of the pressure probes, and on maneuvers, speed, and aircraft attitude. Errors of static air pressure will also propagate to speed calculation. A careful investigation of the errors will result in correction for position error Δp_s, and for errors of attitudes in angles of attack and sideslip. For best results, research aircraft use routinely special devices such as booms or FADS to improve the measurement of important flow parameters. By flight testing, corrections can be achieved for a given configuration of the aircraft. Flight tests apply additional probes or procedures (e.g., tower flyby, trailing cone) to obtain better measurements for static air pressure of the undisturbed air $p_{s\infty}$.

2.5 Static Air Temperature

Temperature is an important variable for describing physical and chemical processes in the atmosphere. An exact knowledge of atmospheric temperature is necessary to understand energy and heat transfer within the Earth system driving the climate and weather systems, to characterize the rate of chemical reactions, and to know the state of aggregation of atmospheric compounds.

2.5.1 Aeronautic Definitions of Temperatures

There are a number of subtleties involved with the measurement of temperature from a fast-moving platform because the actual air temperature is disturbed by the aircraft. From the technical point of view, the following aeronautic definitions of temperature are in common use (Stickney, Shedlov, and Thompson 1994):

i. *Static air temperature* T_s is the temperature of the undisturbed air through which the aircraft is about to fly. Ideally, this should correspond to the usual air temperature T. This is similar to the distinction between common air pressure p and static air pressure p_s.

ii. *Total air temperature* T_t is the maximum air temperature that can be attained by 100% conversion of the kinetic energy (per unit mass of air) of the flight.

iii. *Recovery temperature* (T_r) is the adiabatic value of local air temperature on each portion of the aircraft surface due to incomplete recovery of the kinetic energy.

iv. *Measured temperature* (T_m) is the actual temperature as measured, which differs from T_r because of heat transfer effects due to imposed environments.

All temperature sensors have to be calibrated to a defined temperature scale. More detailed calibration standards to produce the Kelvin or Celsius scale are described in the International Temperature Scale (ITS), 1990 version (ITS-90).

2.5.2 Challenges of Airborne Temperature Measurements

Beside the common problems of high-precision laboratory temperature measurements, airborne temperature measurements involve additional challenges. Temperature probes are exposed to a harsh environment if installed onboard an aircraft. Vibrations can change material properties or even destroy a sensor if no precautions are taken. Vibration of wires or connector contacts can cause additional signal noise in signal lines. Temperature probes and electronics are often exposed to strong temperature gradients or variations of temperature (typically −60 to +50 °C). Temperature gradients can produce a hard-to-detect offset to the signal by inducing a thermoelectric voltage at points where different types of metal are connected with each other (e.g., soldered joint, connector contact), and strong variations of temperature are harmful to most electronics since nearly all electronic components show a temperature dependence in their properties. Pressure changes and the possibility of condensation at the sensor or electronics can cause additional problems.

The most challenging aspect of airborne temperature measurements is the aerodynamic effect of the flow distortion caused by the aircraft and the sensor itself. Each solid inserted into a flow will cause a distortion, changing the pressure, temperature, and density field of the flow. Bernoulli's theorem states that the sum of all forms of energy in a fluid flowing along an enclosed path (a streamline) is the same at any two points in that path. Considering a compressible flow and provided that the steady flow of the gas is adiabatic, we obtain Bernoulli's theorem for a compressible gas.

$$\left(\frac{\gamma}{\gamma-1}\right)\cdot\frac{p_s}{\rho}+\frac{u^2}{2}=\text{constant} \tag{2.17}$$

with p_s, the static air pressure; ρ, the air density; u, the free-stream air velocity; and $\gamma = c_p/c_v$, the adiabatic exponent. c_p = 1004 J kg^{-1} K^{-1} and c_v = 717 J kg^{-1} K^{-1} are the specific heat capacities at constant pressure and volume (both for dry air), respectively. This equation can be rewritten as

$$\frac{u^2}{2}+c_p\cdot T=\text{constant} \tag{2.18}$$

using the ideal gas law for dry air

$$p=\rho\cdot R_{dry}\cdot T \tag{2.19}$$

Here we have the specific gas constant R_{dry} of dry air given by

$$R_{dry}=c_p-c_v=\left(\frac{\gamma-1}{\gamma}\right)\cdot c_p \tag{2.20}$$

At the stagnation point where the flow comes to rest, there is a complete conversion of the energy of motion into thermal energy. The temperature rise, ΔT, in this case can be calculated using Eq. (2.19) from the free air stream temperature T and the free air stream velocity u; hence,

$$\Delta T=\frac{u^2}{2\,c_p} \tag{2.21}$$

Using the definition of the Mach number M as the ratio of the air stream velocity u and the speed of sound c,

$$M = \frac{u}{c} = \frac{u}{\sqrt{\gamma \cdot \frac{p_s}{\rho}}} \quad \textbf{2.22}$$

we can calculate the temperature rise as a function of the Mach number:

$$\Delta T = T \cdot \left(\frac{\gamma - 1}{2}\right) \cdot M^2 \quad \textbf{2.23}$$

As shown in Figure 2.4, the temperature rise at the stagnation point reaches around 1.3 K at an air stream velocity of 50 m s^{-1} (~100 knots) and around 16 K at 180 m s^{-1} (~350 knots).

To allow for the fact that, apart from at the stagnation point, the conversion of the kinetic energy of motion into thermal energy is incomplete, it is common to introduce a local recovery factor r in Eq. (2.21):

$$\Delta T = r \cdot \frac{u^2}{2\,c_p} = T \cdot r \cdot \left(\frac{\gamma - 1}{2}\right) \cdot M^2 \text{ for } r \leq 1 \quad \textbf{2.24}$$

Typical values of r measured for a cylindrical element with its axis orientated normal to the flow are between 0.6 and 0.7 and for a spherical element, around 0.75 (Lenschow and Pennell, 1974).

Figure 2.4 Maximum kinetic temperature rise as function of the airstream velocity (sea level, dry, 0 °C). (Source: Courtesy of Martin Zger.)

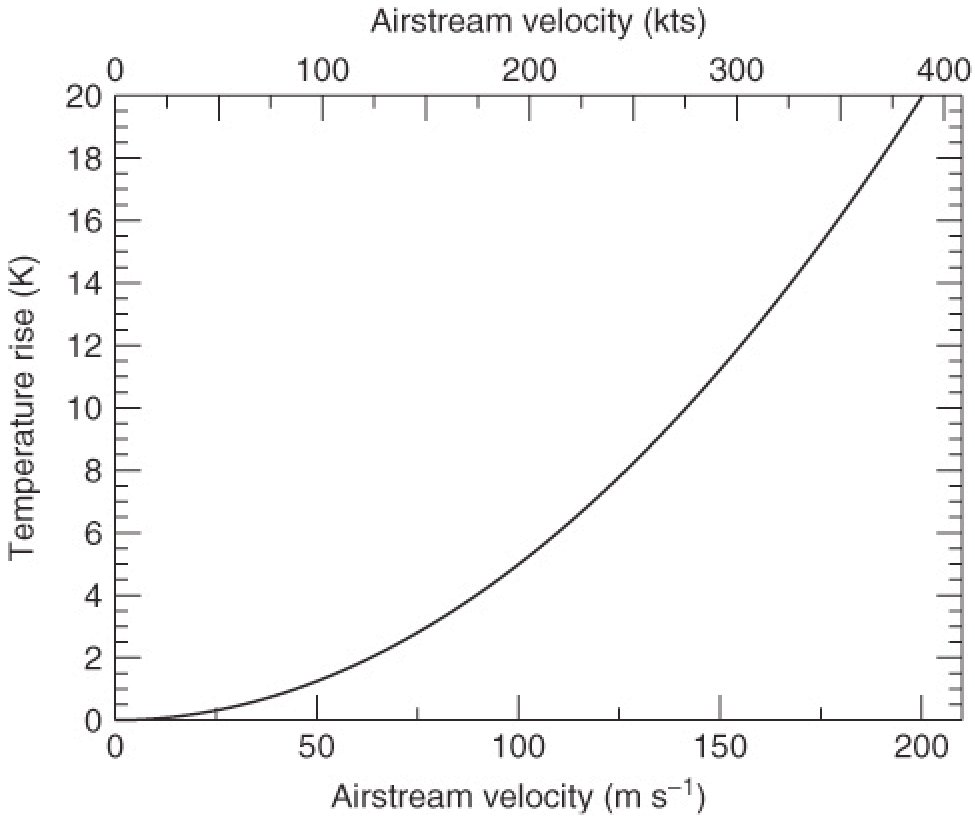

In bringing a temperature sensor onboard an aircraft, the flow distortion caused by both the aircraft and the sensor itself should be considered. Considering the aircraft as a solid surrounded by airflow with the air stream velocity identical to the true airspeed of the aircraft, the temperature field around the aircraft can be described by a field of local recovery factors. The local recovery factors of the temperature sensor and of the aircraft at the position of the sensor interact with each other such that at least the higher value of both will supersede the other. To avoid complex calibration of the combined aircraft/sensor system, either the position of the sensor has to be selected very carefully or the sensor should be designed with a recovery factor very close to 1. Therefore, most commercial aircraft use total air temperature T_t sensors with recovery factors between r = 0.95 and r = 0.99. For scientific temperature measurements, the highest absolute accuracy under normal conditions is still reached using these commercial total air temperature T_t sensors, which are commonly

mounted close to the aircraft nose or on forward-extending booms. In addition to these total air temperature T_t sensors, a wide variety of different contact (immersion) and non-contact-type sensors are also in use.

2.5.3 Immersion Probe

Immersion type temperature sensors are fast-responding instruments (typically in the range of 1 Hz to 1 kHz) and are thus suited to measure the turbulent fluctuations. They are designed for use in a wide range of altitude, weather, and flow speed. The main component of an immersion probe is usually a platinum or nickel resistance sensing element, such as an open wire or a thin coil around a ceramic element. The electrical resistance of the wire is usually assumed to be a linear function of the wire temperature. The sensor is more or less directly exposed to the airflow but the measured temperature is not the required static air temperature T_s. From the previous equations, the static air temperature T_s can be calculated from the measured temperature T_m by

$$T_s = \frac{T_m}{1 + \frac{r \cdot (\gamma - 1)}{2} \cdot M^2} \tag{2.25}$$

with

$$r = \frac{T_m - T_s}{T_t - T_s} \leq 1 \tag{2.26}$$

If data of the Mach number M are not available with high precision, an additional pressure sensor very close to the temperature sensor, measuring total air pressure p_t, allows for the calculation of the static air temperature T_s:

$$T_s = \frac{T_m}{r \cdot \left[\left(\frac{p_t}{p_s}\right)^{\kappa} - 1\right] + 1} \tag{2.27}$$

with

$$\kappa = \left(\frac{\gamma - 1}{\gamma}\right) \tag{2.28}$$

Some manufacturers (e.g., Goodrich, formerly Rosemount) use the recovery correction η instead of the recovery factor r. The recovery correction is defined as

$$\eta = \frac{T_t - T_m}{T_t} \tag{2.29}$$

which is related to r by

$$r = 1 - \eta \cdot \left[1 + \frac{2}{(\gamma - 1) \cdot M^2}\right] \tag{2.30}$$

Depending on the design of the sensor, the recovery factor can depend not only on the Mach number but also on the mounting position and aircraft attitude. In the following, the most common design of immersion type sensors is discussed.

Total air temperature sensors (Figure 2.5a) are designed to achieve a high recovery factor ($r > 0.95$) to minimize the aerodynamic influence of the aircraft and the sensor housing on the temperature measurement. These sensors are commercially available and well characterized by intensive wind tunnel testing. Some designs are also optimized to separate particles such as water droplets or ice crystals from the air stream. The mounting position of these sensors is not relevant as long as the housing is aligned parallel to the local flow field and sources of turbulence (e.g., propellers, other inlets, or antennae) in front of the sensor are absent. Different sensing elements are available, such as open wire elements for fast time response or more robust encapsulated elements. To improve time response, modified sensing elements such as miniature thermistors have been investigated (Friehe and Khelif, 1992).

Figure 2.5 (a) Goodrich (formerly Rosemount) total temperature probe and (b) reverse-flow probe as used on the NSF/NCAR King Air. Air enters through port (A) and is exhausted through port (B) after coming in thermal contact with the platinum wire sensor (C). These probes are designed to separate cloud hydrometeors (D) from the airstream reaching the sensing element. (Source: From Lawson and Cooper (1990). Copyright 1990 American Meteorological Society. Reprinted with permission.)

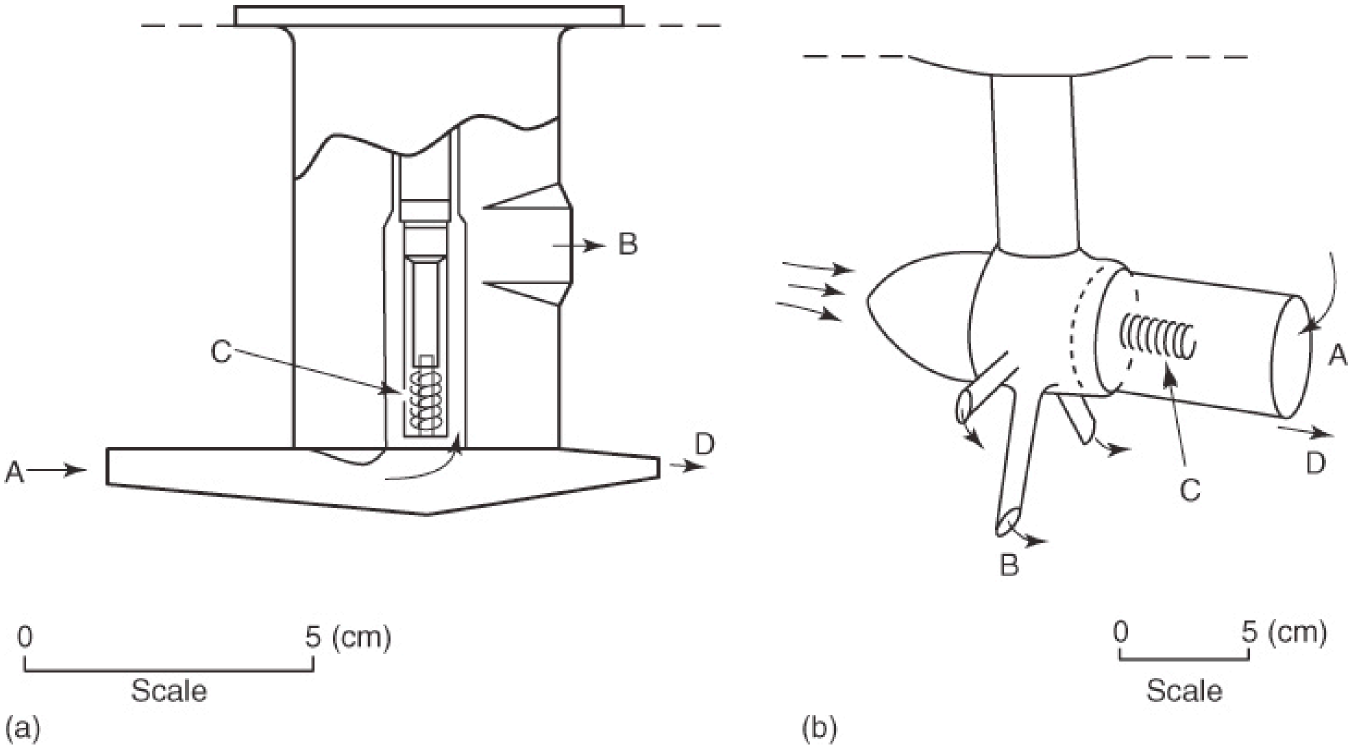

2.5.4 Reverse-Flow Sensor

Several investigations have shown that in heavy clouds, the particle separation of commercial total air temperature sensors may fail and sensor wetting may occur (Lenschow and Pennell, 1974; Lawson and Cooper, 1990; Sinkevich and Lawson 2005). A number of attempts at solving the *in situ* thermometer in-cloud wetting problem are described by Lawson and Cooper (1990) and are all based on some manner of inertially separating the cloud water from the airstream. One approach, initially developed in Canada and at the University of Chicago (Rodi and Spyers-Duran 1972), is the reverse-flow housing, one version of which is shown in Figure 2.5b. This uses exhaust ports that produce a negative pressure inducing the reverse flow through the housing. Lawson and Rodi (1992) and Lawson and Cooper (1990) report tests of the efficacy of the reverse-flow housing using a device at the sensing element location measuring conductivity on a surface that is very sensitive to the presence of liquid water. The conductivity tests clearly indicated that water reached the reverse-flow sensing element, although results from supercooled cloud penetrations, while not as definitive, indicate immunity from wetting. Lawson and Cooper (1990), using wind tunnel observations, suggested that water accumulated and streaming back on the housing may be the mechanism for ingestion of water into the reverse-flow housing, also explaining why the housing is much more effective in supercooled cloud.

2.5.5 Radiative Probe

Air temperature may be derived from measurements of the emitted radiance in the thermal infrared (TIR) spectral region. It is desirable that the weighting function of the detected radiation should be confined within a short distance (~10–100 m) of the detector. This reduces the sensitivity to changes in aircraft attitude, when the viewing path of the instrument may be shifted from the horizontal and may, therefore, view through the vertical temperature gradient of the atmosphere. Suitable wavelengths for measurement are, therefore, strongly absorbed in the atmosphere, and a typical choice is the 4.25 μm absorption band of CO_2 (Beaton, 2006).

The temperature may be determined by inversion of the Planck function that describes the radiance, $B_\lambda(T)$, emitted by a blackbody of temperature T (Chapter 7, Eq. (7.22)). The inversion of the Planck function gives

$$T^{-1} = \frac{k_B \cdot \lambda}{h \cdot c} \cdot \left\{ \ln\left[\frac{2\,h \cdot c^2}{\lambda^5 \cdot B_\lambda(T)} \right] + 1 \right\} \quad \textbf{2.31}$$

with the Boltzmann constant $k_B = 1.3806 \times 10^{-23}$ J K^{-1}; the Planck constant $h = 6.6262 \times 10^{-34}$ J s; T, the absolute temperature in Kelvin; and λ, the wavelength. When the atmospheric path is totally absorbing, and hence its emission is perfect (emissivity is unity), the brightness temperature is equal to the temperature of the air.

A recent implementation of this principle is described by Beaton (2006) (Figure 2.6). The instrument consists of a filter radiometer, with a passband width of ~0.05 μm. A rotating chopper wheel allows the detector to view alternately the atmospheric radiance and the emission from an internal temperature-controlled blackbody target. Measurement of the difference signal and the blackbody temperature allows the atmospheric brightness temperature to be determined.

Figure 2.6 A block diagram of the Ophir air temperature radiometer (2006). The external window is at the right. Behind it is the chopper wheel, the 4.3 μm interference filter, the focusing lens, and then the detector can. Inside the detector can is the HgCdTe detector, the thermistor to monitor the detector temperature, and the thermoelectric cooler for the detector. The TEC driver supplies power to the thermoelectric coolers for the detector and controlled blackbody. The entire optical system is kept near the external air temperature by air circulating between the inner and outer cans of the optical head. (Source: Figure redrawn from Beaton (2006) and used by permission.)

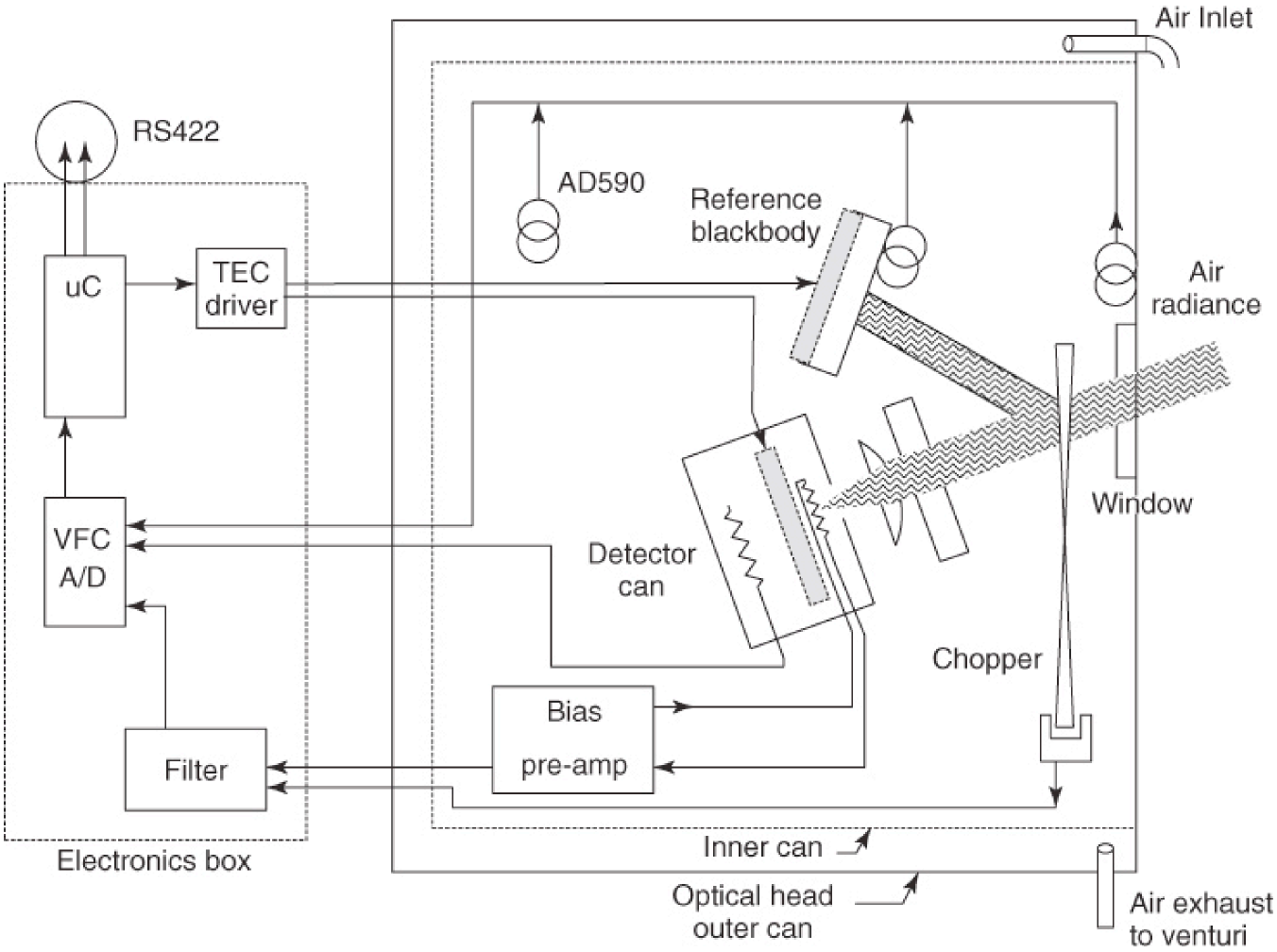

The instrument housing has an external window that is transparent in the TIR. This allows the internal temperature and humidity of the instrument to be more easily stabilized. The window must be maintained free of any materials that are strongly absorbing at the detection wavelength. This includes liquid water that might form a thin film across the window when the instrument is in liquid-phase clouds or rain.

Liquid- and ice-phase clouds are both strongly absorbing at the 4.25 μm wavelength. The impact of this fact when making measurements in cloud is that the absorption within the wings of the passband of the filter is increased compared to that in clear air. This has the effect of decreasing the effective viewing path within cloud from 100 to ~20 m (Beaton, 2006).

In principle, the instrument can be radiometrically calibrated to give an absolute true air temperature measurement. In practice, however, the stability of such calibrations is insufficient and they are normally calibrated against an immersion temperature sensor using cloud-free in-flight data. Such a calibration will typically exclude data from periods when the aircraft roll and pitch angles exclude certain limits. This ensures the rejection of any data obtained when the instrument may be viewing up or down the atmospheric vertical gradient of temperature.

The sample rate of such a radiometric temperature sensor is typically around 1 Hz. At typical flight speeds of 70–100 m s^{-1}, this means that the along-track averaging length is comparable with the instrument viewing path length. Higher-frequency sampling is possible but will increase the noise level.

2.5.6 Ultrasonic Probe

Ultrasonic thermometry is based on the measurement of the speed of sound of the air that mainly is a function of temperature. The speed of sound is derived from the measurement of the transit time of a short sound pulse over a well-known distance. A relative movement of the air with respect to the emitter of the sound pulse (e.g., wind) will be superimposed on the speed of sound. Measuring the transit time back and forth along the same path allows extraction of the speed of sound as well as the wind vector component along the sound propagation path. This principle is widely used for ground-based measurements of 3D wind and temperature simultaneously (Section 2.8.3). Owing to the noncontact type of measurement, a high time resolution is possible, making the method useful for the measurement of temperature fluctuation. But its ability for absolute temperature measurement is strongly reduced by secondary effects in sound wave propagation theory based on the assumption that air is an ideal gas (Cruette 2000). Up to now, only a few ultrasonic temperature probes have been used for airborne measurement, mainly on slow-flying aircraft or helicopters. Calculation of static temperature using this type of probe requires measurement of water vapor mixing ratio because this type of probe measures the sonic temperature, which is closely related to virtual temperature:

$$T_{\mathrm{vir}} = T \cdot \frac{w + \epsilon}{\epsilon \cdot (1 + w)} \tag{2.32}$$

where w is the mixing ratio and ⊠ = $R_{\mathrm{dry}}/R_{\mathrm{wv}} \approx 0.622$ in the Earth's atmosphere. $R_{\mathrm{dry}} = 287.05$ J kg^{-1} K^{-1} is the specific gas constant of dry air, and $R_{\mathrm{vw}} = 461.7$ J kg^{-1} K^{-1} is the specific gas constant for water vapor.

2.5.7 Error Sources

The following error discussion mainly deals with immersion type total air temperature sensors because they are the most common and widely used static air temperature sensors onboard an aircraft. Nevertheless, most points also apply for other types of sensors or give at least a good guideline for a more specific error analysis.

2.5.7.1 Sensor

2.5.7.1.1 Calibration Accuracy

The error discussion of immersion type temperature sensors starts with the basic temperature versus resistance calibration of the sensor element itself. Commercially available calibration systems based on the dry well technique achieve accuracy in the range of 0.2–0.5 K. With more sophisticated stirred immersion bath calibration systems, accuracies better than 0.1 K can be achieved for temperatures above −70 °C. This calibration accuracy includes contributions from many error sources such as bath homogeneity, temporal stability, accuracy of reference, accuracy of fit, accuracy of ohmmeter, and the contribution of contact voltages.

2.5.7.1.2 Conduction and Radiation

The immersion type air temperature senor is based on the heat transfer from the air to the sensor by advection. Whenever temperature gradients between the sensor and its housing or mounting exist, heat transfer to the sensor element by conduction or radiation has to be considered. Possible countermeasures are thermal insulation and radiation shields. Typical total air temperature sensors are constructed so that conduction and radiation errors can be neglected as long as a sufficient airflow across the sensor is guaranteed (Stickney, Shedlov, and Thompson 1994).

2.5.7.1.3 Self-Heating

The typical resistance measurement of an immersion temperature sensor applies a constant current source to the resistor. Within the resistor, electric power is converted into heat influencing the temperature measurement itself. The self-heating effect can either be measured and corrected by, for example, wind tunnel tests or be minimized by keeping the electric power dissipated in the sensor as low as possible.

2.5.7.1.4 Deicing

In order to be able to measure static air temperature T_s during icing conditions and to avoid aircraft damage by ice shedding, some total air temperature probes are equipped with deicing heaters. The deicing heats up the front part of the housing preventing the build up of ice. The heated housing often influences the temperature measurement inside the housing. If known, for example, as a result of wind tunnel testing, this deicing error can be corrected. In-flight calibration procedures can also be used to identify the deicing error. These typically involve making measurements in a region of uniform temperature with and without the deicing heating.

2.5.7.1.5 Time Constant

If not properly addressed, the unknown time response of the sensor can introduce an additional error to the temperature measurement, especially if flying in varying temperature conditions, for example, during ascent and descent. Several approaches have been made to correct the temperature measurement for the known time lag mainly to improve the time response of turbulence measurement and to provide greater accuracy of sensible heat fluxes (Rodi and Spyers-Duran, 1972; McCarthy, 1973; Inverarity, 2000).

2.5.7.2 Dynamic Error Sources

As stated, the flow distortion caused by the aircraft and the sensor itself can strongly influence the static air temperature measurement. Figure 2.4 shows that this dynamically induced error becomes significant for airspeeds above ~20 m s^{-1}. If not using a well-characterized total air temperature probe, extensive wind tunnel testing or airflow simulation is necessary to distinguish the dynamic correction. Commercially available total air temperature probes often provide all information necessary to correct the dynamic error. Stickney, Shedlov, and Thompson (1994) published a recovery correction for different types of Rosemount total air temperature probes derived from wind tunnel experiments. The remaining dynamic error resulting from production tolerance and the repeatability error of the wind tunnel tests are in the range of 0.2 K. The Mach number dependence of the recovery correction cannot be neglected for Mach numbers ≥ 0.4. Using a constant recovery factor instead of the Mach-number-dependent recovery correction would introduce an additional error of a few tenths of a Kelvin.

2.5.7.3 In-Cloud Measurements

Typical total air temperature probes as well as special reverse flow sensors are designed to separate particles from the airstream avoiding contamination of the sensor element. Nevertheless, erroneous temperature measurements in clouds in the range of a few Kelvin have been documented (Lenschow and Pennell, 1974; Lawson and Cooper, 1990; Sinkevich and Lawson, 2005). Lawson and Cooper (1990) identified evaporative cooling of the wetted sensor as a possible reason for the measurement error in clouds and quantified the evaporative cooling effect for a completely wetted sensor. By comparing in-cloud temperature measurements of a Rosemount total air temperature probe with a radiative probe, Lawson and

Cooper (1990) found that the full evaporative cooling effect applies only at very high liquid water content. For lower liquid water contents, partial wetting of the sensor or housing will lead to a cooling effect that is difficult to quantify (Lawson and Rodi, 1992).

2.5.8 Calibration of Temperature Sensors

Laboratory calibration of temperature sensors is restricted to the calibration of the sensor element itself. As mentioned earlier, sophisticated stirred immersion bath calibration systems can achieve overall accuracies better than 0.1 K. Depending on the bath fluid in use, a temperature range of −70 to +50 °C is achievable. Extensive error analysis of the whole calibration chain as well as traceability to national standards is necessary to achieve the aforementioned accuracy.

To avoid extensive wind tunnel testing, most non-total-air-temperature-type sensors as well as radiative probes rely on in-flight calibration and are, therefore, used together with a well-characterized total air temperature probe. Under cloud-free and stable conditions, both instruments are compared against each other, yielding a correction factor valid for these particular flight conditions. A fully independent characterization of the temperature probe requires extensive flight testing to quantify the dependencies on Mach number, density, and attitude (pitch, roll, yaw). Nevertheless, the achievable accuracy of in-flight calibration is always limited to the accuracy of the reference sensor. If no reference sensor is available, special flight test maneuvers can be used to determine the recovery factor. From Eq. (2.25) it follows that plotting the measured temperature as a function of the Mach number will yield the static air temperature, T_s, as the coordinate intercept. From the slope of this curve, together with T_s, the recovery factor, r, can be calculated. However, the absolute accuracy of this method is limited by the temporal stability of T_s as well as by the fact that a constant recovery factor is assumed.

2.5.9 Summary, Gaps, Emerging Technologies

Huge efforts have been made in the past decades to improve airborne static air temperature measurements. Nevertheless, most reliable and accurate measurements still are based on standard commercial total air temperature probes. Currently, the achievable absolute accuracy is around half a Kelvin for cloud-free conditions. Future scientific demands mainly focus on higher absolute accuracy, especially within clouds where, for example, temperature accuracy is a limiting factor on the accuracy of estimates of supersaturation. Some research is underway to develop optical temperature probes, mainly for military purposes. These instruments are currently in the stage of proof of concept with bulky laboratory installations. Expected accuracies are in the range of 0.3 (optimal conditions) to 1.2 K (clouds).

2.6 Water Vapor Measurements

This section is dedicated to Cornelius Schiller. With the development of FISH, the "Fast In situ Stratospheric Hygrometer," in the 1990s, Cornelius Schiller started a new era of the measurement of water vapor under the challenging conditions of the upper troposphere and lower stratosphere (UT/LS). Accurate water vapor measurements under such conditions are exceedingly difficult, but Cornelius together with a few colleagues succeeded in pushing the boundaries of science and technology by taking measurements with this instrument on multiple platforms, from the tropics to high latitudes. FISH is considered to be one of the most accurate hygrometers in the world. Today, FISH represents a reference for water measurements around the world on a variety of platforms in the UT/LS. Cornelius strongly fostered utilization of high-flying research aircraft as an important platform to study atmospheric processes in the UT/LS region. As a result of this activity, he was strongly engaged in EUFAR (European Facility for Airborne Research) and particularly in what the future fleet of European research aircraft will look like. Cornelius' research resulted in a large number of high-quality publications with great impact on the scientific community. Although at times his work has necessarily been quite technical, his motivation remained always very clear: striving for scientific truth and a better understanding of the Earth's atmosphere and climate. He led large international measurement campaigns, and we all followed him because of his strong scientific integrity combined with his kind and congenial nature. Cornelius Schiller, our dear colleague and friend, passed away on 3 March 2012 in Neuss, Germany, after he lost his fight against cancer. We will not forget him, but continue to work in his spirit on the questions that he raised.

2.6.1 Importance of Atmospheric Water Vapor

Water vapor plays a key role in the atmospheric energy budget and greenhouse effect. Water vapor is one of the key drivers for and key tracers of atmospheric transport, and as a source of the hydroxyl radical, it has a strong influence on the chemistry (i.e., oxidative capacity) of the atmosphere. Water vapor is the source of clouds and precipitation and is crucial in the removal of aerosol particles or water-soluble gases through heterogeneous reactions with aerosol or cloud particles. Water vapor has a strong influence on the size distribution of hygroscopic aerosol particles and their optical properties, that is, atmospheric radiative effects. Therefore, airborne measurements of ambient water vapor are important in many areas of atmospheric research.

Important considerations for an airborne hygrometer are fast time response for adequate spatial resolution, insensitivity to the presence of liquid water or ice particles, demonstrated insensitivity to contamination from instrument or platform surfaces, capability of measuring ice supersaturation, ease of calibration, and sensitivity over a wide dynamic range. Water vapor levels drop from a few parts per hundred at the ground to a few parts per million in the lower stratosphere. For this reason, many different measurement methods and sensors have been developed through the years, each having certain advantages and limitations and each being suitable for some but not all applications. There is a long history of water vapor measurements using various techniques.

This section describes the different types of humidity measurement techniques that are in airborne use today, their advantages and limitations, and the applications where certain instruments should or should not be used.

2.6.2 Humidity Variables

In the atmosphere, water generally can exist in three states (thermodynamic phases): as frozen ice crystals, as liquid water droplets, and as gaseous water vapor. Important variables for humidity measurements are the water vapor (partial) pressure and the saturation vapor pressures that can be in equilibrium with either the liquid or the ice phase. Only at the triple point of water, all three phases coexist in thermodynamic equilibrium, and then the (saturated) vapor pressure of both ice and liquid water is $e_{s,\ tri} = 611.657$ Pa at the triple point temperature of $T_{tri} = 273.16$ K (Guildner, Johnson, and Jones, 1976). The transition between gaseous phase and the liquid or ice phase increases in an exponential fashion with temperature T at the surface of the transition. The Clausius–Clapeyron equation that describes the nonlinear dependence of the saturated vapor pressure e_s on temperature T may be written as (Rogers and Yau, 1989)

$$\frac{de_s}{dT} = \frac{e_s \cdot l^*}{R_{wv} \cdot T^2} \tag{2.33}$$

where l^* represents either the specific latent heat of evaporation $l_v \approx 2.501 \times 10^6$ J kg^{-1} or sublimation $l_s \approx 2.835 \times 10^6$ J kg^{-1}, and $R_{wv} = 461.7$ J kg^{-1} K^{-1} is the specific gas constant for water vapor. Although l_v and l_s are both temperature dependent, in the first approximation, the Clausius–Clapeyron equation can be integrated by regarding the latent heat as constant in order to give an expression for the saturation vapor pressure over liquid water ($T \geq T_{tri}$) or an ice surface ($T \leq T_{tri}$) as a function of temperature, that is,

$$e_s(T) = e_{s0} \cdot \exp\left[\frac{l^*}{R_{wv}} \cdot \left(\frac{1}{T_0} - \frac{1}{T}\right)\right] \tag{2.34}$$

where e_{s0} is the value of saturation vapor pressure at temperature T_0. At $T_0 = 0$°C, $e_{s0} = 611$ Pa.

Equation (2.34) shows that the saturation vapor pressure e_s is a strong function of temperature T and increases almost exponentially with increasing temperature. At temperatures below the triple point temperature T_{tri}, next to the stable ice phase, a transient metastable supercooled liquid phase may exist under certain conditions such that at the same temperature the saturation water vapor pressure is higher over the liquid than over the ice (Murphy and Koop, 2005). In this case, one can measure the dew point temperature, that is, saturation with respect to liquid water, or the frost point temperature, that is, saturation with respect to ice. Supercooled liquid water can be expected in clouds down to temperatures as low as ~235 K.

Equation (2.34) is not an exact fit because water vapor is not an ideal gas and the latent heats of evaporation and sublimation are temperature dependent. This finding is directly related to the temperature dependence of the specific heat

capacity of water vapor, ice, and supercooled water. There are several saturation water vapor equations to calculate the equilibrium pressure of water vapor over a plane surface of liquid water or ice as a function of temperature (Sonntag, 1994; Murphy and Koop 2005).

Several measures can be used to express the water vapor abundance in the atmosphere (Rogers and Yau, 1989). The most important ones are the (partial) water vapor pressure, the molar or mass density of water vapor, specific humidity (the ratio of the mass of the water vapor to the mass of the moist air), the mass mixing ratio (the ratio of the mass of water vapor to the mass of dry air), and the volume mixing ratio (the ratio of the water vapor pressure to (total) ambient air pressure). Other measures often used are the dew point or the frost point (temperature), defined as the temperature at which the air parcel would be saturated with respect to liquid water or ice, respectively. Atmospheric water vapor abundances are also frequently reported as the relative humidity, RH (ratio of the actual water vapor pressure e to the saturation pressure, e_s, at the prevailing ambient air temperature, T, multiplied by 100%). RH can be expressed with respect to the liquid water or the ice phase.

The calculation of saturation ratios and relative humidity from water vapor partial pressures critically depends on the ambient gas temperature because of the saturation pressures being exponential functions of T. Relative changes with temperature T are about 6% K^{-1} at 300 K and increase to about 15% K^{-1} at 200 K. Therefore, not only accurate water vapor measurements but also accurate ambient air temperature measurements are needed.

2.6.3 Dew or Frost Point Hygrometer

The dew or frost point hygrometer is the most widely used instrument to measure atmospheric water vapor concentration onboard a research aircraft. The chilled mirror technique in its basic form (Figure 2.7) detects the dew or frost point by cooling a small reflective metal surface or mirror in contact with ambient air until a layer of dew (liquid droplets) or frost (ice crystals) begins to form. Formation of dew or frost on the mirror is detected optically with a light-emitting diode (LED) illuminating the mirror and one or more photodetectors that sense the change in light reflecting or scattering when dew or frost forms on the mirror. The signal is fed into an electronic feedback control system to regulate the mirror temperature through cooling and heating, to the point where dew or frost just starts to form. A temperature sensor, usually a thermistor, is embedded within the mirror surface to measure its surface temperature. When a predetermined layer of dew or frost is maintained on the mirror surface, the measured mirror temperature corresponds to the dew or frost point of the ambient air flowing over the mirror. A comprehensive overview of chilled mirror hygrometers is given by Wiederhold (1997).

Figure 2.7 Block diagram of a chilled mirror hygrometer. The LED is the light source and the two photodetectors sense the scattered (PD-1) and reflected light (PD-2) from the mirror to determine if dew or frost is present or not. The ratio of the two detector signals determines if mirror heating or cooling is required.

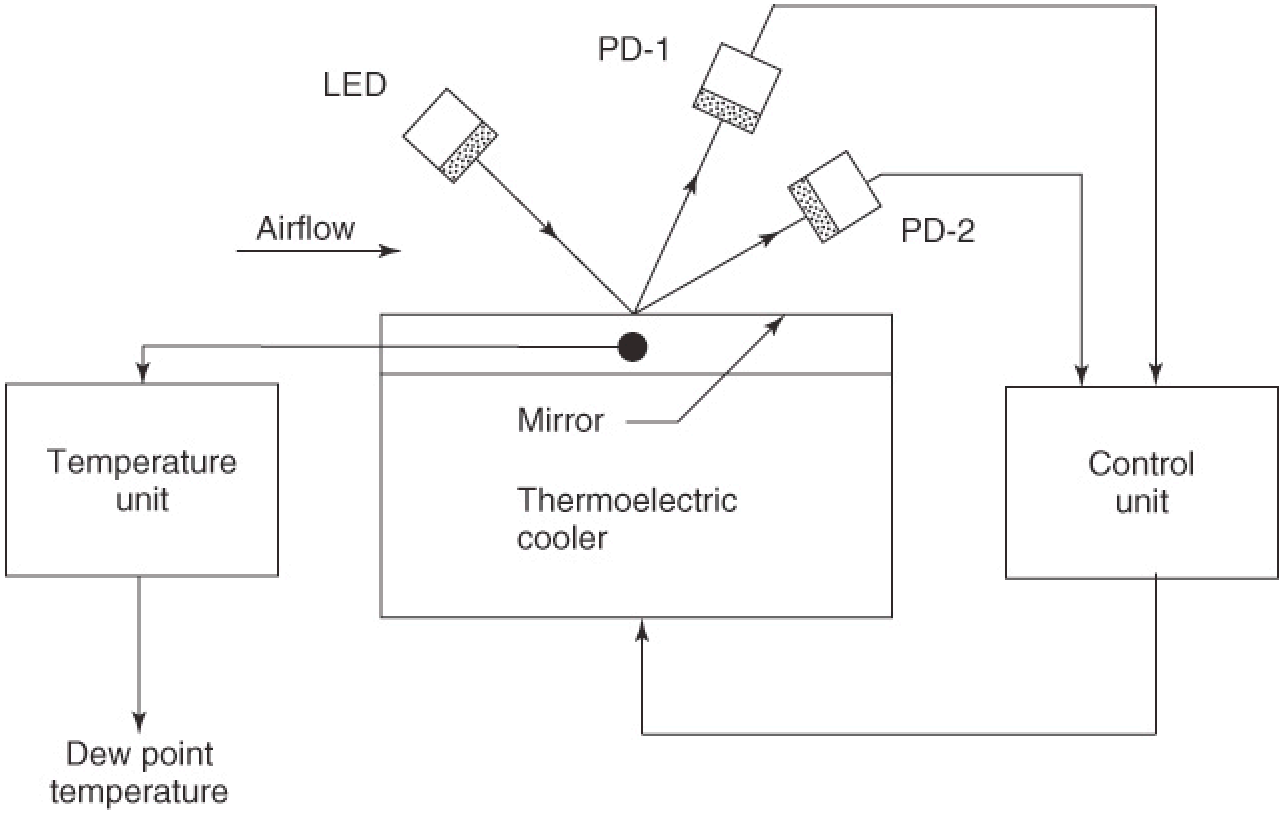

For airborne applications in the lower or middle troposphere, the thermoelectrically cooled mirror type is most widely used. Thermoelectric coolers are small and inexpensive and work over a modest range of dew or frost point temperatures down to approximately −40 °C for single-stage and −60 °C for two-stage thermoelectric coolers. However, their capabilities at low humidities (frost point temperatures below −50 °C) are limited. At the low end of their range, they become increasingly inefficient and slow to respond. At low humidities, that is, frost point temperatures below −50 °C, cryogenic cooling of the mirror is preferred.

In the cryogenic chilled mirror hygrometer, the mirror is cooled by a freely boiling cryogen, such as Freon or nitrogen, through an attached rod of high thermal conductivity. The mirror is permanently cooled to a temperature well below its measurement range. To make a measurement, the mirror temperature is raised to the dew or frost point and maintained at that point by a servo-controlled electrical heater. Most airborne cryogenic dew or frost point hygrometers in use nowadays are based on the original balloon-borne design made by Mastenbrook (1968) and have been modified for airborne use (Spyers-Duran, 1991; Buck, 1991; Ovarlez and Velthoven, 1997). Since the mid-1990s, commercial instruments became available (Busen and Buck, 1995). The efficient cooling allows operation down to frost point temperatures of −90 °C and faster response than feasible with thermoelectric cooling. In the more advanced instruments, a continuously operating stirling cycle cryogenic refrigerator or cryopump is used, allowing for continuous operation at very low frost points.

The chilled mirror method may seem to be a fundamental technique of measuring the dew or frost point temperature with a very accurate and well-calibrated temperature sensor (accuracy better than ±0.1 °C), but this type of hygrometer is influenced by several factors that can have a large and significant impact on the quality and reliability of the performance of the instrument (Wiederhold, 1997). Among the factors are instability of the feedback controller, air temperature variations, dew or frost point ambiguity between 0 and −30 °C, and the presence of water-soluble contaminants on the mirror (the Raoult effect).

The dew or frost point hygrometer is capable of quasi-continuous operation to measure dew or frost point temperature with an accuracy varying from 0.5 to 2°C. It is often difficult to determine when or if a chilled mirror is operating correctly, particularly when ambient conditions are changing rapidly (e.g., when entering a cloud). Dew or frost point devices typically have slow responses.

A lightweight miniaturized application of a dew or frost point hygrometer is the surface acoustic wave (SAW) hygrometer that uses a tiny piezoelectric crystal to detect the onset of condensation. The intrinsic sensitivity of the SAW to mass loading changes is a result of the propagation of the acoustic wave occurring only on the surface of the crystal. This increased sensitivity means that theoretically, SAW hygrometers have fast response times and can operate in very dry environments (Hansford 2006).

Another version of the dew or frost point hygrometer uses basic components similar to those shown in Figure 2.7, but differs in its ability to measure the water vapor mixing ratio in the high RH range of about 95–105% (Gerber, 1980). This version, termed *saturation hygrometer*, is based on the observation by Wylie, Davies, and Caw (1965). The accuracy of the saturation hygrometer was estimated to be ~0.02% RH near ambient RH = 100%, 0.1% at RH = 99%, and 0.6% at RH = 97% in radiation fog measurements (Gerber, 1991b).

2.6.4 Lyman-α Absorption Hygrometer

The Lyman-α absorption hygrometer uses the water vapor absorption of vacuum ultraviolet (VUV) light in a narrow optical band around the Lyman-α emission line of atomic hydrogen at a center wavelength of 121.56 nm. While for Lyman-α light water vapor absorption is very strong, oxygen absorption is uniquely low, and most other common gases are relatively transparent, for example, nitrogen. A significant fraction of radiation is absorbed over a few millimeters path length under normal conditions. The response is very fast, on the order of milliseconds. Developments in the Lyman-α absorption hygrometers for airborne use have been made by Buck (1985), Weinheimer and Schwiesow (1992), and others. The Lyman-α absorption hygrometer in its basic form is shown in Figure 2.8.

Figure 2.8 Single-beam Lyman-α absorption hygrometer.

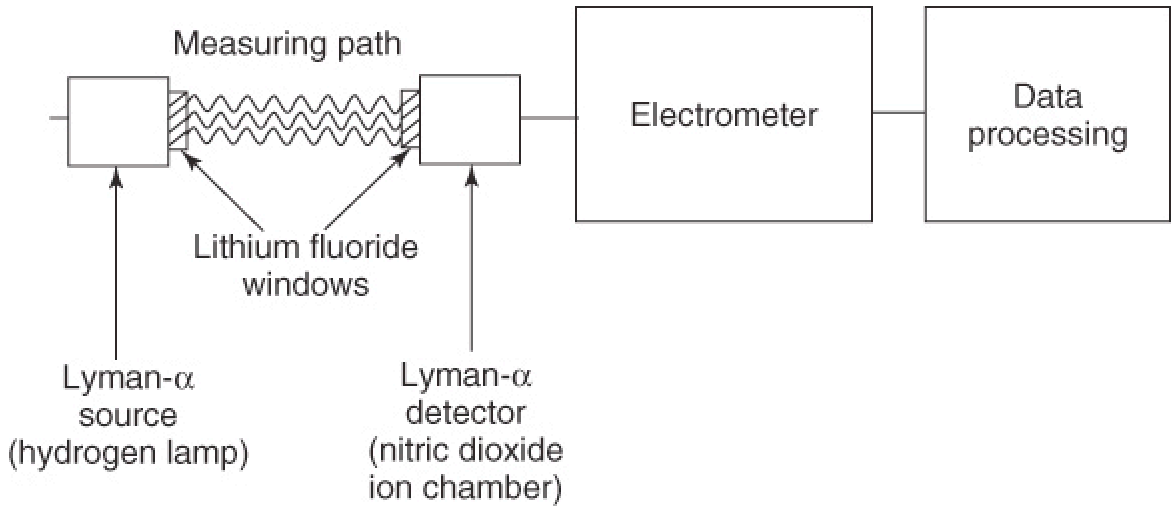

The Lyman-α absorption hygrometer is a secondary measurement device and must be regularly calibrated, usually in the laboratory in an enclosed airflow circuit with a chilled mirror hygrometer as calibration standard. When a reference hygrometer is not available, a variable path length self-calibration technique can be used (Buck, 1976). The Lyman-α absorption hygrometer for airborne use has been made commercially available by Buck Research Instruments (although production was stopped at end of 1990s). The device offers a very fast response (≈5 ms), and can measure water vapor densities of 0.1–25 g m^{-3} with a relative precision of 0.2% and an accuracy of 5%. The fast response makes it a suitable instrument for ultrafast hygrometry (sample rates of 10–100 Hz), water vapor flux measurements, or micrometeorological measurements inside and outside clouds.

It is not possible to use the Lyman-α absorption hygrometer alone to measure absolute water vapor density; the Lyman-α light source aging and optical window contamination are the main factors that prevent a stable predictable calibration. Therefore, in practice, a chilled mirror hygrometer is simultaneously used for slow accurate dew point measurements (Friehe, Grossman, and Pann, 1986).

2.6.5 Lyman-α Fluorescence Hygrometer

This type of hygrometer uses the Lyman-α light absorption in conjunction with the photodissociation of H_2O molecules, whereby fluorescence light is emitted and used as a measure of the H_2O abundance. The method was developed by Kley and Stone (1978) and Bertaux and Delan (1978). Figure 2.9 shows the schematics of the Lyman-α fluorescence hygrometer that consists of a monochromatic Lyman-α light source, two VUV detectors (VUV_A and VUV_B) to measure the Lyman-α light intensities, and a photomultiplier to measure OH-fluorescence light intensity.

Figure 2.9 Lyman-α fluorescence hygrometer after geometry by Kley (1979). QW, quartz window; VUV-A, NO cell A; VUV-B, NO cell B; PM, photo multiplier.

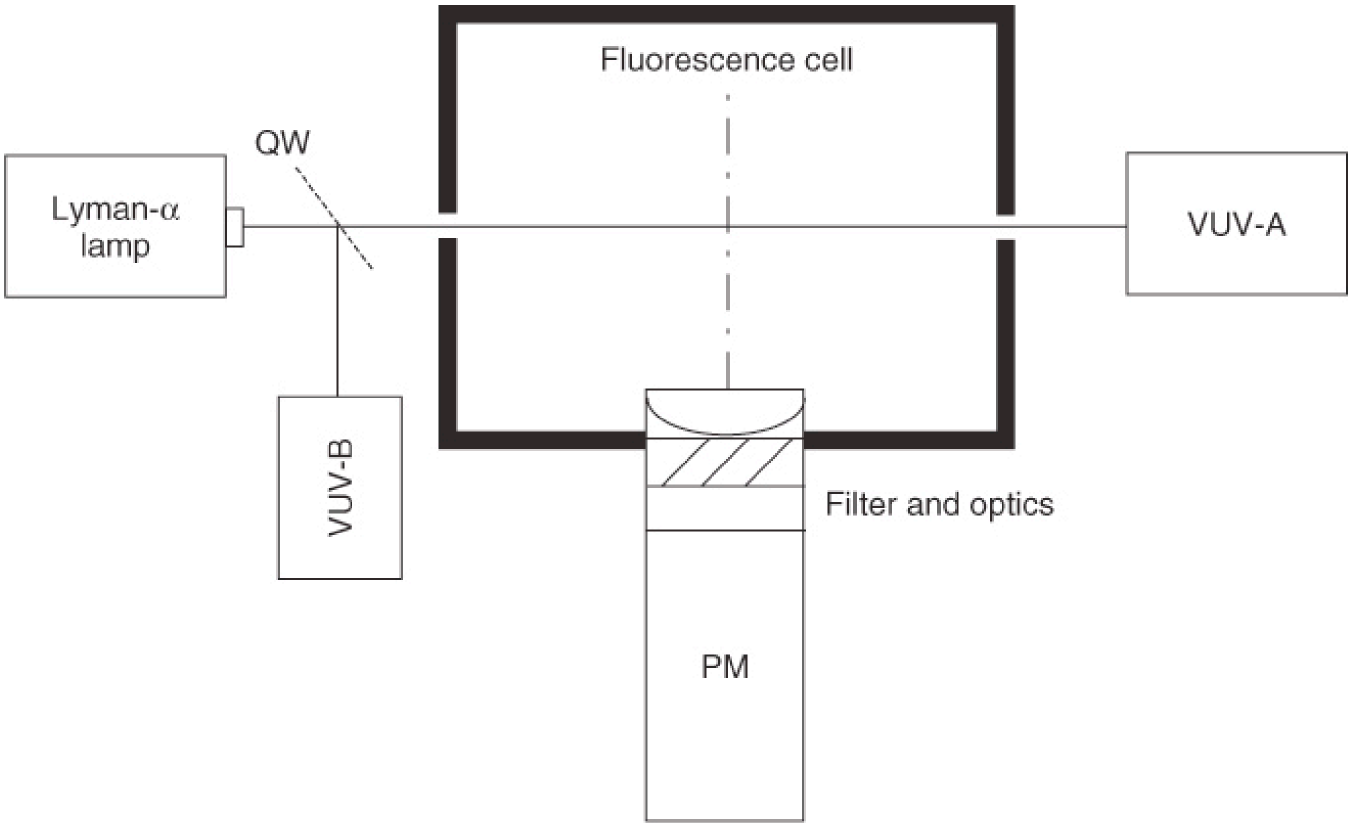

The Lyman-α fluorescence technique can achieve a large dynamic range for measurements from the middle and upper troposphere at about 1000 μmol mol^{-1} into the dry stratosphere with only 2–5 μmol mol^{-1}, where changes on the order of 0.1 μmol mol^{-1} can be detected with a relative uncertainty of ±5%. Although it is more usual practice for the volume mixing ratio to be expressed in terms of ppm, or ppmv, these are nonstandard units, and for the purpose of this text, we have used μmol mol^{-1} for ppm or ppmv. Large flow rates through the hygrometers together with integration times on the order of 1 s enable the measurement of small-scale features in the atmosphere.

Only a few well-established Lyman-α fluorescence hygrometers for use on research aircraft exist, such as the NOAA Aeronomy instrument developed by Kley and Stone (1978) and Kley (1979), the Harvard instrument (Weinstock 1994, 2009), the FISH (Fast In Situ Stratospheric Hygrometer) instrument (Zöger 1999; Schiller 2008), and the UK Met Office instrument (Keramitsoglou 2002). Although the principle of operation is the same, the instrumental layout of each instrument is different. The fluorescence technique needs laboratory calibration, but in-flight calibration can be achieved by combining Lyman-α fluorescence with direct Lyman-α absorption measurements of water vapor (Kley 1979).

2.6.6 Infrared Absorption Hygrometer

The IR absorption hygrometer uses the absorption of IR radiation by water vapor at certain distinct wavelength bands (e.g., Hyson and Hicks, 1975). Usually a dual-wavelength differential absorption technique is applied, whereby one

(primary) wavelength is subject to strong water vapor absorption and the other (reference) is not. An example of a single-beam absorption hygrometer with one IR source and one IR detector is shown in Figure 2.10.

Figure 2.10 Schematic of a typical implementation of a single-beam IR absorption hygrometer.

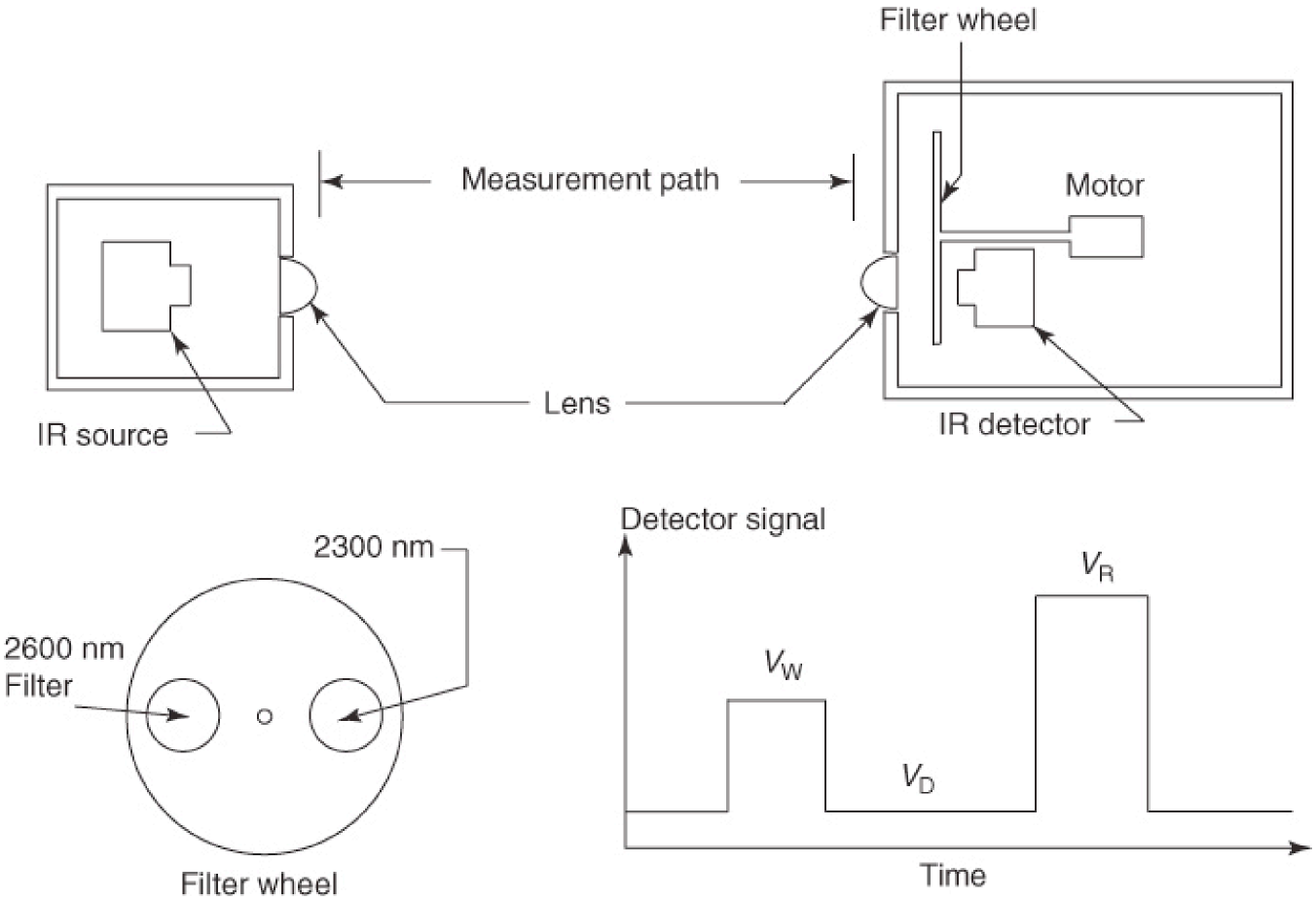

Two IR band filters, one in the reference band (e.g., 2.3 μm wavelength) and the other in the absorbing band (e.g., 2.6 μm wavelength) are mounted on a chopper wheel that rotates into the IR light beam in front of the IR detector. The detector signal would be composed of three components (Figure 2.10) sampled when the absorbing filter, no filter, and the reference filter are in the beam, respectively. This yields a normalized signal that is a direct measure of the abundance of water vapor, and at the same time is insensitive to drifts, deposits on the optical windows, and haze or fog within the sample volume. Through the use of lock-in (i.e., phase-sensitive) detection techniques, a high sensitivity of 0.01 g m^{-3} and sample rates of 20 Hz can be obtained (e.g., Ohtaki and Matsui, 1982; Cerni, 1994). Nowadays, a suite of extractive as well as open-path instruments have become commercially available, mostly designed for fast and simultaneous measurements of CO_2 and H_2O concentrations. The measurement range is thereby about 0.3–30 g m^{-3}, such that airborne use is limited to the lower part of the troposphere.

2.6.7 Tunable Laser Absorption Spectroscopy Hygrometer

Tunable laser absorption spectroscopy (TLAS) is based on the use of a narrow-band, wavelength-tunable diode laser source to scan one or more characteristic spectral absorption lines of the target trace gas, here water vapor, in the path of the laser beam. A basic TLAS hygrometer (Figure 2.11) consists of a tunable diode laser, optical absorption cell with sample gas, and a photodiode as detector. The transmitted light intensity can be related to the concentration of the absorbing water vapor by the Lambert–Bouguer law (also called *Beer's law*); see also Section 7.2.5. A comprehensive overview of TLAS is given by Heard (2006).

Figure 2.11 Basic setup of tunable laser absorption spectrometer (TLAS).

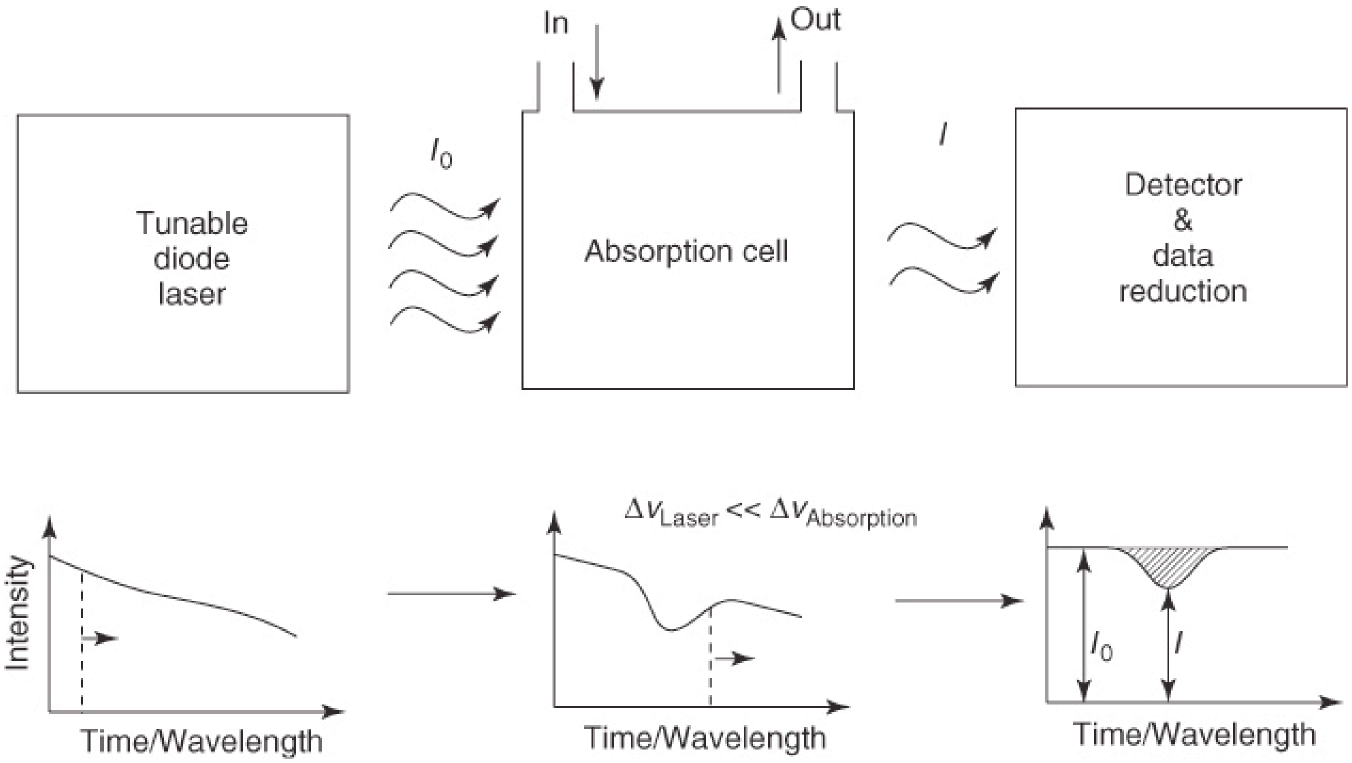

In the past two decades, development of tunable diode lasers has yielded devices operating at around room temperature, particularly in the 1–2 μm wavelength band where water vapor has strong absorption lines. Communication laser diodes have become available, which allow the use of very compact, robust, and lightweight instruments. Furthermore, through the use of a multipass absorption cell, where the optical beam is reflected back and forth between a set of mirrors, a larger optical path length is obtained that offers higher sensitivity in a fairly compact system (Heard, 2006; May, 1998; Diskin 2002; Zondlo 2010). In conjunction, often a 2f-modulation technique is used to increase the sensitivity even further. However, this requires regular and precise calibrations in the laboratory.

If regularly calibrated, a TLAS hygrometer system can achieve relative accuracies of about 5–10% with a precision of ~ 2–3%. Most advanced instruments can even achieve this in the sub-μmol mol^{-1} range of 1–10 μmol mol^{-1}. Developments in the new TLAS hygrometer systems, which use direct absorption, are in progress (Gurlit 2005). These new instruments measure water vapor in the lower range of 1000 μmol mol^{-1} down to a few μmol mol^{-1} or even lower. They use a new self-calibrating data evaluation strategy based on the first principles approach and known parameters such as the absorption line strength, pressure, gas temperature, and absorption path length. This strategy may provide a very robust, compact, lightweight, highly accurate, and absolute laser hygrometer without the need for regular recalibration.

2.6.8 Thin Film Capacitance Hygrometer

Capacitive humidity sensors are miniaturized sensors that measure dielectric changes of thin films resulting from water vapor uptake as they come into equilibrium with the water vapor pressure in the surrounding air. In the scope of the Measurement of Ozone and Water Vapor by Airbus In-Service Aircraft (MOZAIC) project, this type of humidity sensor is deployed on board commercial aircraft to measure relative humidity in the troposphere (Helten 1998). The humidity sensing element (Humicap) together with a PT100 resistor to measure temperature is mounted in a total air temperature housing (Figure 2.12a), which protects the sensors against particles and avoids any wall contact of the sampled air. Although capacitive humidity sensors are widely deployed on radiosondes, their use on aircraft in the middle and upper troposphere requires careful and regular calibrations.

Figure 2.12 (a) Cross-sectional view of the airborne capacitive sensing element in air sampling total air temperature housing; control holes are for boundary layer and right angle causes particle separation. (b) Mean vertical profiles of Mach number, difference between total air temperature (TAT) and static air temperature (SAT): $T_t - T_s$, and ratio of static and dynamic relative humidity (RH_S/RH_D) for subsonic high-flying aircraft as obtained from MOZAIC measurements (1998).

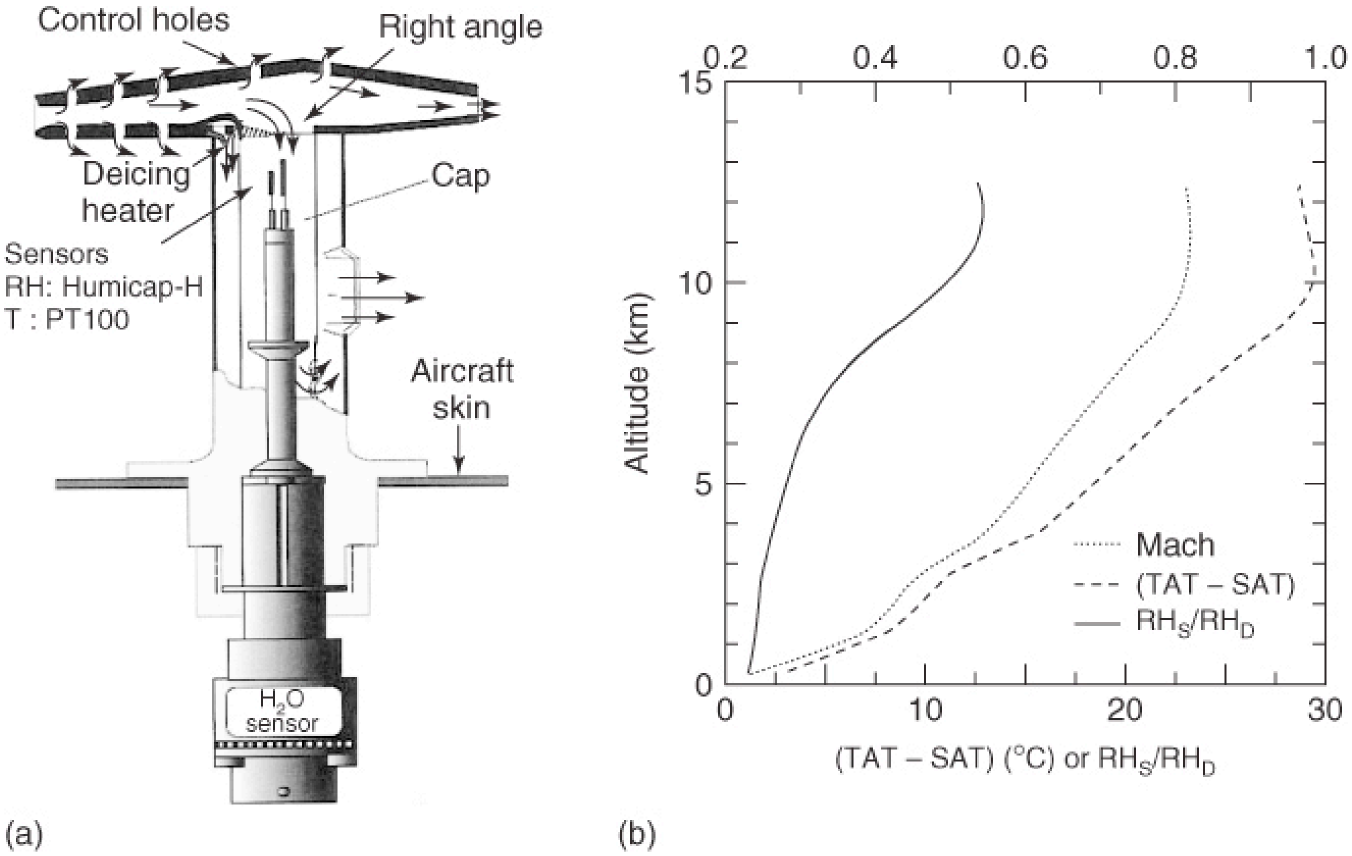

The air entering the total air temperature housing is subject to adiabatic compression caused by the strong speed reduction in the inlet part of the housing. The adiabatic compression produces an appreciable temperature rise relative to the ambient static air temperature T_s if the aircraft speed is comparable to the speed of sound. For a fast high-flying aircraft, the resulting difference between total and static air temperature ($T_t - T_s$) increases from 2 K near ground to ~30 K at 10–12 km cruise altitude (Figure 2.12b). Because of the strong temperature increase, the dynamic relative humidity RH_D detected by the sensing element in the total air temperature housing is appreciably lower than the static relative humidity of the ambient air, RH_S (Helten 1998). We thus obtain

$$RH_s = RH_D \cdot \left(\frac{T_s}{T_t}\right)^{\frac{c_p}{c_p - c_v}} \cdot \frac{e_s(T_t)}{e_s(T_s)} \quad \textbf{2.35}$$

where $e_s(T_s)$ and $e_s(T_t)$ are the water vapor saturation pressures of liquid water at static air temperature T_s and total air temperature T_t, respectively. c_p = 1004 J kg^{-1} K^{-1} and c_v = 717 J kg^{-1} K^{-1} are the specific heats of dry air at constant pressure and volume, respectively. Therefore, for a fast high-flying aircraft, the sensor operates in the lowest 10% of its full dynamic range ($RH_S/RH_D > 10$), and it is obvious that individual calibrations of each sensor are necessary. This fact is not adequately covered by the factory calibration provided with the transmitter unit and hence requires regular individual recalibration of each sensor.

The response time of the humidity sensor is dependent on the polymer's ability to adsorb and desorb water vapor and on the sensor design, and it is strongly dependent on the temperature of the sensor. The time response of the sensor in the lower or middle troposphere is good (1–10 s) but increases at lower temperatures to values of about 1 min at ambient air temperatures of −60 °C. The sensor is sensitive to chemical contamination by either additional bonding of the nonwater

molecules or reduction in the ability of the polymer to adsorb water molecules, which may cause either a dry bias or reduce the sensitivity of the sensor, respectively. Regular calibration and cleaning of the capacitive sensor is a prerequisite for proper performance.

Long-term experience in MOZAIC has demonstrated that if the capacitive sensors are carefully calibrated every 500 h of flight operation, uncertainties better than ±(4–6)% RH for measurements between the surface and 12 km can be obtained (Helten 1998, 1999; Smit 2008). For measuring stratospheric humidity, where relative humidities well below 5% prevail, the uncertainty of the capacitive humidity device is insufficient for quantitative water vapor measurements.

2.6.9 Total Water Vapor and Isotopic Abundances of ^{18}O and ^{2}H

A special airborne application is the measurement of total water vapor, that is, the sum of gaseous phase and vaporized liquid or ice phase. The air is sampled by a forward-facing inlet tube mounted outside the aircraft, while the contribution of liquid or ice phase is forced to evaporate by heating before detection. The gas and particle sampling characteristics for the inlets of the different research aircraft are approximated by computational fluid dynamics modeling (Chapter 6). Usually, gaseous water vapor content is measured simultaneously and independently in order to derive from the difference of both measurements the liquid or ice water content of clouds (Weinstock (2006); Schiller (2008)). A more detailed overview is given in Chapter 6, Section 6.4.

Measurements of relative isotopic abundances of ^{17}O, ^{18}O, and ^{2}H in atmospheric water vapor constitute a complementary and powerful proxy to study various processes in which atmospheric water vapor is involved (Moyer 1996). The traditional way is to use cryogenic techniques to trap water vapor in the atmosphere into samples that are measured subsequently off-line with laboratory-based isotope-ratio determination by mass spectroscopy (Zahn, 2001; Franz and Röckmann, 2005). A detailed introduction to water sampling for isotopic analysis, including scientific examples, are given in Chapter 3. While mass spectroscopy can provide high-precision measurements, cryogenic trapping requires long sample times, particularly in dry conditions. This reduces the spatial resolution of the measurement with the speed of the aircraft, such that small spatial structures such as isolated clouds cannot be resolved. The use of tunable diode laser spectroscopy techniques such as TLAS (Webster and Heymsfield, 2003; Dyroff, Fuetterer, and Zahn, 2010) and cavity ring-down spectroscopy (CRDS) (Kerstel 2006; Sayres 2009a) enables *in situ* measurements of water vapor isotope ratios also to be performed. Another challenging technique to detect isotopic ^{2}H abundance at low humidities is using the photodissociation of water vapor followed by laser-induced fluorescence detection of the OH fragment (HOxtope) (St Clair 2008). With these new *in situ* measuring devices, sampling times can be reduced by more than a factor 20 to achieve similar performance compared to the conventional off-line sampling techniques (Dyroff, Fuetterer, and Zahn, 2010).

2.6.10 Factors Influencing In-Flight Performance

Numerous factors can influence the in-flight performance of airborne water vapor measurements. To mention them all is beyond the scope of this chapter. Of crucial importance are the sticking of water vapor at surfaces and the appropriate use of sampling systems.

2.6.10.1 Sticking of Water Vapor at Surfaces

Water molecules are highly polar, such that water molecules attach themselves tenaciously to surfaces. Particularly, at low temperatures, this can lead to large memory effects of the water vapor measurements. Additional heating may eliminate any such memory effects. The selection of hydrophobic materials is an important part of the sampling and measuring system design of the hygrometer. In general, to avoid any water vapor contamination or memory effect from the aircraft skin, it is most favorable that the air inlets are sampling air outside the aerodynamic boundary layer at the aircraft skin. In addition, moisture must not be allowed to leak into the measurement system or interfere with the measurements. This is most critical in dry regions or at low humidities in the upper troposphere and stratosphere.

2.6.10.2 Sampling Systems

Most airborne hygrometers use extractive sampling systems that force the sampled ambient air through an appropriate inlet system into a closed-path detector system installed inside the aircraft. Usually the sideward or backward facing type of air inlets are deployed by using a pump, and the forward directed type of air inlets use the ram pressure caused the moving aircraft. Some special hygrometer designs use measuring systems located outside the aircraft, such as fast Lyman-α or IR absorption hygrometers, or open-path TLAS systems. These open-path systems have the advantage of virtually eliminating contamination issues and removing the requirement for a reference instrument for in-flight calibration, but they require ambient air temperature and pressure measurements. Furthermore, at high speed, this type of measurement is sensitive to any flow disturbances that may lead to poorly defined pressure and temperature conditions within the measuring section of the open-path system.

2.6.11 Humidity Measurements with Dropsondes

A dropsonde, or dropwindsonde, is a compact meteorological device that is released from high-flying aircraft. While descending (speed of ~10 m s^{-1}) through the atmosphere on a special balloon-like parachute, continuous measurements of pressure, temperature, relative humidity, and horizontal wind velocity and direction are made and transmitted by radiotelemetry to the aircraft for further onboard data processing (Figure 2.13a).

Figure 2.13 (a) GPS dropsonde descending on its parachute. (b) GPS dropsonde and internal view.

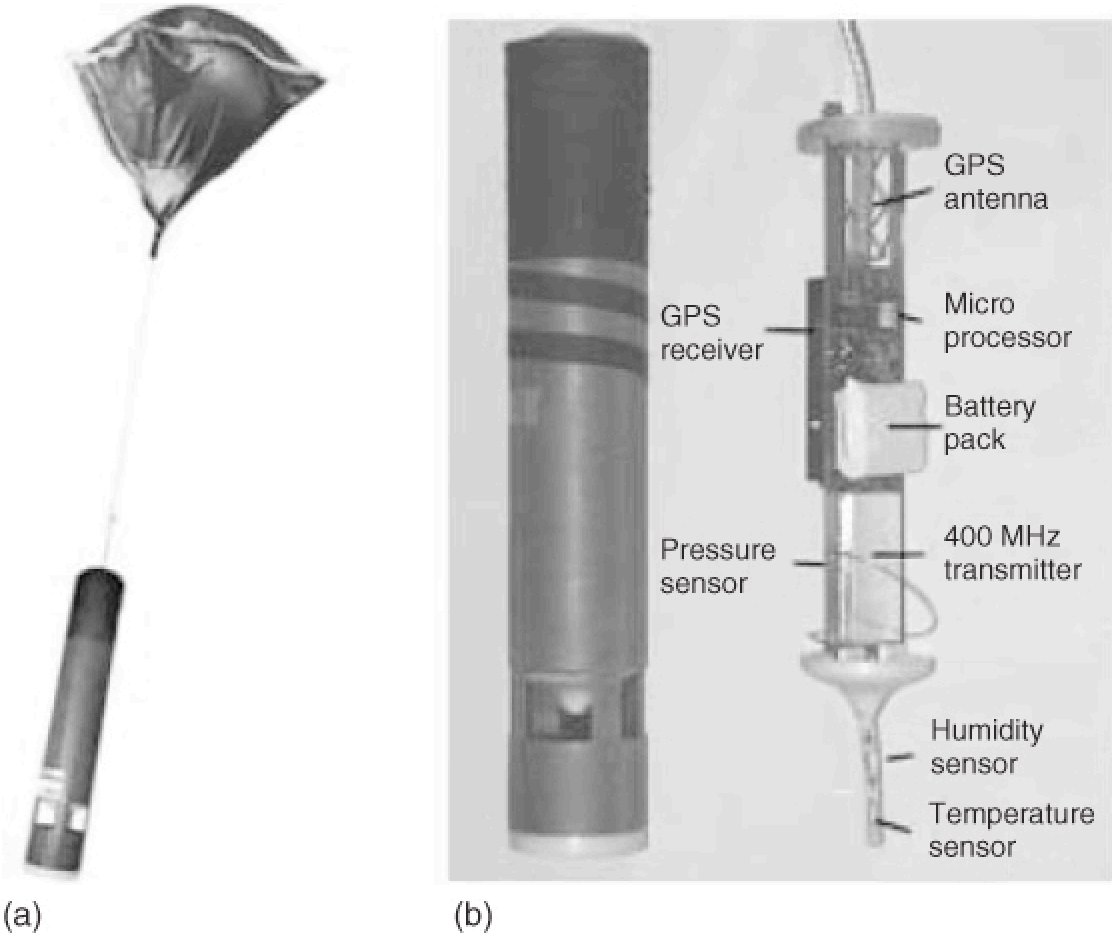

Dropsondes, an adaption from radiosonde technology (Dabberdt 2002), were first developed in the 1960s for hurricane reconnaissance and forecasting purposes. Since then the dropsonde technology has been further developed at the NCAR (Boulder, USA), see for example Govind (1975). The latest major achievement in dropsonde technology is the NCAR GPS dropwindsonde (Hock and Franklin, 1999). The wind-finding capability of the dropsonde is based on the GPS satellite navigation, while pressure, temperature, and relative humidity sensors (all capacitive) are the same as used in radiosondes (model type RS92) manufactured by Vaisala (Finland).

The dropwindsonde consists of four major components: the pressure, temperature, relative humidity (PTU) sensor module; the digital microprocessor circuitry; the GPS receiver module; and the 400 MHz radio transmitter (Figure 2.13b). Relative humidity is measured by the H-Humicap, the same type of capacitive thin film sensor as deployed in the capacitance hygrometer (Section 2.6.8). Artifacts in the measurements caused by condensation and icing can be avoided through the use of two sensors operating on a preprogrammed heating cycle: while one sensor measures ambient relative humidity, the second sensor is heated and allowed to recover. The sondes are manufactured in license by Vaisala (Finland), and thousands of them are flown every year for hurricane reconnaissance and other atmospheric research purposes.

2.6.12 Calibration and In-Flight Validation

Essential for an accurate and reliable humidity measurement is regular calibration against an accurate reference instrument, sometimes called a *transfer standard*, that operates on fundamental principles and is capable of providing stable and accurate results. Most widely used transfer standards are chilled mirror hygrometers. Thereby, it is important that each transfer standard is traceable to a primary standard. The primary standard, which relies on fundamental principles and base units of measurements, is very accurate, but cumbersome, expensive, time consuming, and thus not applicable in practice. Only a few national standard laboratories have the availability of a primary standard. A detailed description of different calibration techniques and procedures used by national standard laboratories are given by Wiederhold (1997). General guidelines for calibration of atmospheric humidity instruments are given by the World Meteorological Organization (1983).

While the accuracy of these standards has been well established under atmospheric pressure, they have not been validated at the low pressures under which the most controversial water vapor measurements have to be made, in the UT/LS. Also, instruments that might be checked and validated under ideal laboratory conditions might be subject to unknown biases and systematic errors under flight conditions. The AquaVIT water vapor intercomparison, discussed below, made a significant effort in addressing this issue.

In addition, it is essential to validate the performance of different airborne hygrometers through intercomparison with other airborne hygrometers under realistic measurement conditions. This is especially important for those instruments that measure low humidities in the UT/LS. Particularly, at the lowest range of 1–10 μmol mol^{-1}, water vapor observations show large uncertainties, as was noted by the comprehensive 2000 SPARC Assessment of Upper Tropospheric and Stratospheric Water Vapor (2000). It includes intercomparisons of satellites, aircraft, balloon-borne, and ground-based water vapor instruments. Since the report of the World Meteorological Organization (1983), discrepancies remained between key instruments such as Harvard–Lyman-α (Weinstock 2009), FISH–Lyman-α (Zöger 1999; Schiller 2008), and (Jet Propulsion Laboratory) JPL–TLAS (May, 1998). For example, from aircraft intercomparisons during the AURA–MLS (Microwave Limb Sounder) satellite validation (Read 2007), the key instruments showed discrepancies of 10–20% or more at low water vapor values (≤ 10 μmol mol^{-1}). Particularly large differences were observed at temperatures below 190 K. A major laboratory intercomparison was the AquaVIT Water Vapor Intercomparison campaign (https://aqua-vit.icg.kfa-juelich.de/WhitePaper/AquaVITWhitePaper_Final_23Oct2009_6 MB.pdf), where a large number of hygrometers were compared to each other under controlled pressure, temperature, and humidity conditions typical of the UT/LS. Generally, the UT/LS hygrometers such as Harvard–Lyman-α, FISH–Lyman-α, and JPL–TLAS showed agreement within ±10% in the water vapor range of 1–150 μmol mol^{-1}, whereas the Harvard–Lyman-α tended to larger readings at lower water vapor values. These differences observed at low water mixing ratios were of the same character but significantly smaller than those exhibited in flight intercomparison campaigns. However, AquaVIT does not address atmospheric sampling issues, which primarily affect the in-flight performance and have to be addressed separately.

2.6.13 Summary and Emerging Technologies

Airborne measurement of atmospheric humidity has been and continues to be a challenging task. Airborne humidity measurements require continuous care, regular maintenance, and intensive calibration. There is no airborne sensor available that can cover the full dynamic range of water vapor levels from a few percentage near the surface down to a few μmol mol^{-1} in 15–20 km altitude. A survey of different techniques and their performance in terms of time response, precision and accuracy, and specific airborne applications is presented in Table 2.5. While a broad spectrum of instruments exists today, all of them have their limitations, making it necessary to combine several instruments to achieve the required data quality.

Table 2.5 Survey of Different Water Vapor Sensing Techniques and their Specifications of Performance for Airborne Use

Sensor type	Altitude range	Measured quantity	Measured range	Time response	Accuracy	Reliability	Limitations
Dew–frost point [thermoelectric cooling]	LT, MT, and UT	Dew–frost temperature	230–300 K	LT: few seconds UT: few minutes	0.2–0.5 K	Good	Ambiguity dew and frost point 233–273 K
Dew–frost point [cryogenic cooling]	LT, MT, UT, and LS	Dew–frost temperature	185–300 K	10–20 s	0.2 K	Good	Ambiguity dew and frost point 233–273 K
Lyman-α absorption	LT and MT (open path)	Density	0.1–25 g m^{-3}	5 ms	5%	Light source short lifetime; regular cleaning of optic windows needed	Requires in-flight calibration
Lyman-α fluorescence	MT, UT, and LS	Volume mixing ratio	1–1000 nmol mol^{-1}	1 s	5%	Very good	Only for dedicated mission; requires high expertise
IR absorption	LT and MT	Density	0.3–30 g m^{-3}	5 ms	1 g m^{-3}	Sensitive to aircraft vibrations and fast pressure changes	Interferences with large aerosol loadings
IR absorption (closed path)	LT and MT	Density	0.3–30 g m^{-3}	1 s	0.1 g m^{-3}	Good	Interferences with large aerosol loadings
TLAS (open path)	MT, UT, and LS	Density	0.005–1 g m^{-3}	5 ms (20 Hz)	5% (1 Hz)	Good	Only for dedicated mission; requires high expertise
TLAS (closed path)	LT and MT	Density	0.05–30 g m^{-3}	2 s	5–10%	—	For dedicated and in-service operation
CRDS	LT and MT	Density	0.1–30 g m^{-3}	10–30 s	5–10%	—	—
Thin film capacitance [Humicap]	LT, MT, and UT	Relative humidity	0–100% RH	LT: 1 s MT: 10 s UT: 1 min	5% RH	Good, when regularly calibrated	Not suitable for LS
Dropsonde [Humicap]	LT, MT, and UT	Relative humidity	0–100% RH	LT: 1 s MT: 30 s UT: 5 min	5–10% RH	Good	Slow response in UT; not suitable for LS

[a]LT, lower troposphere; MT, middle troposphere; UT, upper troposphere; LS, lower stratosphere.

Substantial improvements in the performance of airborne water vapor measuring systems or new aircraft applications are in progress, particularly through new developments in the field of tunable diode laser spectroscopy. New developments of tunable diode laser spectroscopic techniques are on their way, such as CRDS, a direct absorption technique based upon the gradual decrease of light intensity as a tunable diode laser light pulse undergoes multiple reflections between two highly reflective mirrors in an optical cavity (Berden and Engeln, 2009). An introduction to CRDS and related methods is given in Chapter 3, Section 3.5.3. In the next decade, good performance at low atmospheric humidities (1–100 µmol mol^{-1}) can be expected. Also new airborne applications using CRDS hygrometry to measure, for example, isotopic abundances of ^{17}O, ^{18}O, and ^{2}H in atmospheric water vapor to identify their sources and sinks are becoming feasible (Berden and Engeln, 2009).

Laser-induced photoacoustic spectrometry (LPAS) uses the physical effect that the absorption of periodically modulated laser light can generate a sound wave at the frequency of the light modulation and is proportional to the concentration of the absorbing compound. The dynamic range (or the measurement range) of a photoacoustic instrument is rather large, so that five to six orders of magnitude change in concentration can be achieved (Bozoki, Pogány, and Szabó, 2011). In general, in order to achieve stable relative accuracies of 10% or better, a photoacoustic hygrometer needs to be regularly calibrated.

Advanced instrumental developments of the CIMS (chemical ionization mass spectroscopy) detection techniques enable water vapor measurements at extremely low stratospheric values.

2.7 Three-Dimensional Wind Vector

The three-dimensional (3D) wind vector needs to be measured to characterize large-scale atmospheric motions. We distinguish here between motions on scales on the order of 10 or 100 m and above, and the velocity fluctuations at smaller scales that can be considered turbulence; the latter is covered in Section 2.8. The use of research aircraft to measure mean wind components and vertical eddies has been evolving quite greatly in the past few decades. The techniques to measure

wind and large-scale turbulence by means of airborne instrumentation are (i) the aircraft's response to wind (Lenschow, 1976), (ii) remotely sensed wind measurement using Doppler wind Light Detection and Ranging (LIDAR) (Bilbro 1984a; Bilbro 1986), and (iii) *in situ* wind measurement. The last technique remains the most accurate method and is the subject of this section.

2.7.1 Airborne Wind Measurement Using Gust Probes

Measuring the wind components from moving platforms is a challenge since both ground speed and airspeed of the aircraft are about one order of magnitude larger than the meteorological wind, and errors arise from compressibility, adiabatic heating, and flow distortion. Basic principles of wind measurement from aircraft have been given by Axford (1968) and Lenschow and Stankov (1986).

2.7.1.1 True Airspeed (TAS) and Aircraft Attitude

The horizontal wind speed and direction are computed by the vector sum of the true airspeed (TAS) and the ground relative velocity of the aircraft. The TAS from instrumented aircraft is usually measured by means of gust probes, which can be either installed on nose or wing-tip booms or directly radome mounted. Gust probes are equipped with dynamic, static, and differential pressure ports from which the TAS and the flow angles can be calculated, allowing for the computation of the wind components.

The most common gust probe in use today is the so-called FHP (Figure 2.14). In the FHP, the local wind vector in the aircraft coordinate system is determined from the dynamic pressure increment Δp_q and the pressure differences between four opposite pressure holes in the FHP, that is, the pressure difference in the horizontal plane $\Delta p_\beta = p_2 - p_4$, and in the vertical plane $\Delta p_\alpha = p_1 - p_3$, where p_j, with $j = 1,\ 2,\ 3,\ 4,\ 5$, denotes the individual holes of the FHP, with p_5 being the central hole. The pressure differences Δp_α and Δp_β increase when the angle of attack α and the angle of sideslip β increase. But the pressure differences also depend on the airspeed (and therefore on both the dynamic pressure increment Δp_q and the Mach number) and on the air density ρ (and therefore on the altitude z). Therefore, these pressure differences can be used for both the TAS and aircraft attitude measurements. Calibration routines, both for wind tunnel experiments and flight maneuvers can be found in the literature by Haering (1990); Wörrlein (1990); Haering (1995); Barrick (1996); Friehe (1996); Khelif, Burns, and Friehe (1999); Weiß, Thielecke, and Harders (1999); Williams and Marcotte (2000); van de Kroonenberg (2008); and van de Kroonenberg (2009). For details of the principle of the FHP, see Section A.1, given in the Supplementary Online Material provided on the publisher's web site.

Figure 2.14 Schematic illustration of an FHP showing the pressure ports p_1 to p_5 (head-on perspective, i.e., starboard is on the left side from this point of view).

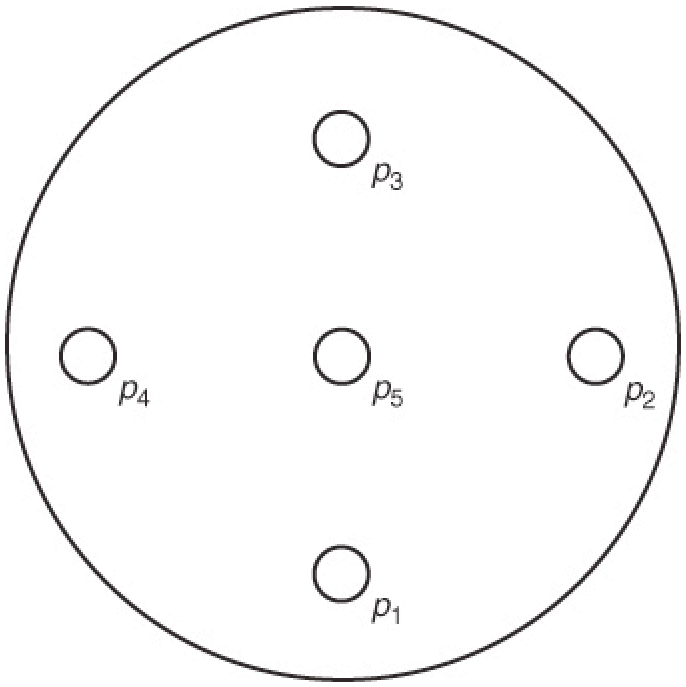

The angles of attack and sideslip (α and β, respectively) are defined as the flow angles with respect to the longitudinal axis of the aircraft in the lateral and vertical directions. These angles along with the TAS define the velocity vector relative to the aircraft. The calculation of airspeed and flow angles is based on the measurement of the surface pressure distribution (Brown, Friehe, and Lenschow, 1983) on the nose of the aircraft itself, from which the angles of attack and sideslip, and the dynamic pressure are obtained. Examples of such instruments are the Best Aircraft Turbulence (BAT) probe, an effort by the NOAA Atmospheric Turbulence and Diffusion Division (ATDD) and that can be installed on slow aircraft; the Aventech Aircraft Integrated Meteorological Measurement System (AIMMS-20) (Foster, 2003); and the FHP by Rosemount that can also be used on fast aircraft. The relative ground speed and the aircraft attitude determination (Euler angles) are described in Section 2.3.

2.7.1.2 Wind Vector Determination

The wind vector can be determined through the following logical progression:

i. TAS calculation,

ii. flow angles calculation,

iii. rotation matrices, and

iv. ground speed calculation.

At each stage, the measured variables must be corrected for undesired airflow distortion as explained later in this section.

The meteorological wind vector $\boldsymbol{v}$ (in the Earth coordinate system) is the difference between the velocity vector of the instrument or sensor $\boldsymbol{v}_{\text{sensor}}$ in the Earth-fixed coordinate system and the TAS vector $\boldsymbol{v}_{\text{TAS}}$ (Lenschow and Stankov, 1986; Lenschow and Spyers–Duran, 1989):

2.36 $$\boldsymbol{v} = \boldsymbol{v}_{\text{sensor}} - \boldsymbol{v}_{\text{TAS}} = \boldsymbol{v}_{\text{aircraft}} + \boldsymbol{v}_{\text{AS}} - \boldsymbol{v}_{\text{TAS}}$$

$\boldsymbol{v}_{\text{sensor}}$ can be expressed as the sum of two velocity components, namely, the speed $\boldsymbol{v}_{\text{aircraft}}$ of the aircraft reference point (the location of the inertial reference system, IRS) and a relative speed $\boldsymbol{v}_{\text{AS}}$ of the sensor with respect to this point caused by changes in the aircraft attitude. $\boldsymbol{v}_{\text{AS}}$ can be calculated from the aircraft rotational velocity vector ω and the distance vector $\mathbf{r}_{\text{AS}}$ between aircraft reference point and the flow sensor in an aircraft-fixed coordinate system:

2.37 $$\mathbf{v}_{\text{AS}} = \omega \times \mathbf{r}_{\text{AS}}$$

Different coordinate systems are used in the wind calculation since some of the data measurements are referenced to the aircraft (gust probe data) and some to an Earth-based coordinate system (IRS data). Therefore, two main coordinate systems are important in the measurement of wind speed, namely, the Earth-fixed (geodetic) coordinate system (x_g, y_g, z_g) and the aircraft-fixed (body) coordinate system (x,y,z). Three Euler angles are used to describe the relative orientation of these two coordinate systems to each other: aircraft yaw (ψ), pitch (θ), and roll (ϕ) angles. The definition of the coordinate systems and the transformation matrices between them are subject to national and international standards, which are commonly available (ANSI, 1992; DIN, 1990).

The TAS as the speed of an aircraft with respect to the air in which it is flying is completely based on pressure data from the gust probe and meteorological parameters such as air temperature, pressure, and humidity. The respective formula can be directly derived from the Bernoulli equation, the ideal gas law, and the adiabatic equation. We thus obtain

$$\mathrm{TAS} = \sqrt{2 \cdot \left(\frac{k}{k-1}\right) \cdot R \cdot T_s \cdot \left[\left(\frac{p_t}{p_s}\right)^{\frac{k-1}{k}} - 1\right]} \tag{2.38}$$

with adiabatic index k, gas constant R for humid air, static air temperature T_s, total air pressure p_t, and static air pressure p_s of the undisturbed air.

The TAS wind vector $\boldsymbol{v}_{\mathrm{TAS}}$ is usually measured in two steps. First, the absolute value $|\boldsymbol{v}_{\mathrm{TAS}}|$ = TAS is determined using Eq. (2.38). It is important to note that the TAS wind vector is normally not aligned with the gust probe due to changes in the aircraft angle of attack and the influence of wind. Especially for slow aircraft, this deviation can be significant. Therefore, the accuracy of the TAS calculation depends strongly on the proper parameterization of the angular dependency of the total and static air pressure measurement (see later discussion). The second step is the measurement of the angles of attack and sideslip between the airflow vector and the gust probe axis. A typical TAS probe is the FHP, see Section A.1, given in the Supplementary Online Material provided on the publisher's web site.

2.7.1.3 Baseline Instrumentation

Two main sensor configurations are commonly used for flow angle measurements. The first one uses the aircraft radome as a sensor, equipped with appropriate flush-mounted pressure ports. This method has the advantage of short tubing between pressure sensors and the gust probe, which guarantees fast response and avoids damping and resonance effects along these lines. This design is also very insensitive to mechanical vibration. However, the aircraft weather RADAR, which is typically located aft of this installation, puts some restrictions on the pressure port design. The determination of the inlet location on the typically nonsymmetric radome and the disturbed pressure field in this area require extensive airflow simulation and in-flight calibration. Another disadvantage is the lack of a proper static pressure port close to the probe.

The second configuration uses a nose boom to locate a flow sensor ahead of the aircraft in order to minimize the effects of aircraft-induced pressure disturbance. If the probe is equipped with a static air pressure port, static source calibration becomes easier and no delay effects between the different pressure sources have to be accounted for. The boom is usually inclined in order to compensate the mean aircraft angle of attack. However, there are serious restrictions to the installation. The intention of bringing the sensor as far ahead of the aircraft as possible (in order to leave the aircraft-induced pressure disturbance) is limited by aeroelastic considerations and the boom natural frequency.

Recent developments have shown that the advantages of both methods can be combined in a boom solution where the pressure sensors are located directly behind the flow sensor at the tip of the boom. This requires a very stiff boom construction as well as specially modified compact pressure sensors (Crawford and Dobosy, 1992; Cremer, 1999).

Pressure sensors for airborne flow measurements must be of high accuracy, small, light, fast and inert to the environmental conditions on the aircraft. The desirable absolute accuracy is 0.1 hPa, which requires regular calibration and an accurate reference. The optimum acquisition rate for these measurements is given by the pneumatic response time of the system. A typical value is 100 Hz, which requires response times of some milliseconds for the sensor itself. Since the most critical parameter of a pressure measurement is temperature, the sensors should be actively temperature controlled in order to withstand an environment that can range from +70 to −70 °C (e.g., on a jet). Thermal error corrections based on measured sensor temperature are subject to systematic errors when the outside temperature changes. The sensitivity to aircraft accelerations can be minimized by choosing an appropriate orientation of the sensor with respect to the aircraft axes.

The second important measurement for the calculation of wind speed is the position and attitude of the gust probe in an Earth-fixed coordinate system. This is usually accomplished using an IRS. Owing to the high costs of these systems, data from the aircraft IRS is often used for this. Time delays and data steps due to internal processing and correction schemes, the Schuler effect, and data drift are possible effects that have to be treated when processing the data (Lenschow and Spyers-Duran, 1989; Matejka and Lewis, 1997). At present, off-the-shelf stand-alone systems are available, which combine accurate low-speed GPS information with data from a fast IMU by applying sophisticated filter techniques. Some systems are even able to use real-time DGPS.

2.7.1.4 Angles of Attack and Sideslip

As mentioned, the two flow angles measured by the gust probe are used to determine the orientation of the TAS vector, one of the two vectors needed to directly determine wind speed. The angle of attack α is the angle between the projection of the airflow vector onto the x, z-plane of the aircraft coordinate system and the aircraft x-axis itself. The angle of sideslip β is defined as the angle between the airflow vector and the aircraft x, z-plane (Boiffier, 1998; Luftfahrtnorm, 1970). Since the free-stream flow lines are bent due to the influence of the aircraft, the local flow angles at the gust probe location are biased (Figure 2.15).

Figure 2.15 The angle of attack can usually not be measured directly by a gust probe, even if the sensor is perfectly characterized. This is due to the flow disturbance caused by the aircraft itself and a possible angular offset between the axes of the aircraft and the flow sensor. When flying at a constant level in a stable atmosphere, the angle of attack is identical to the aircraft pitch as measured by the IRS.

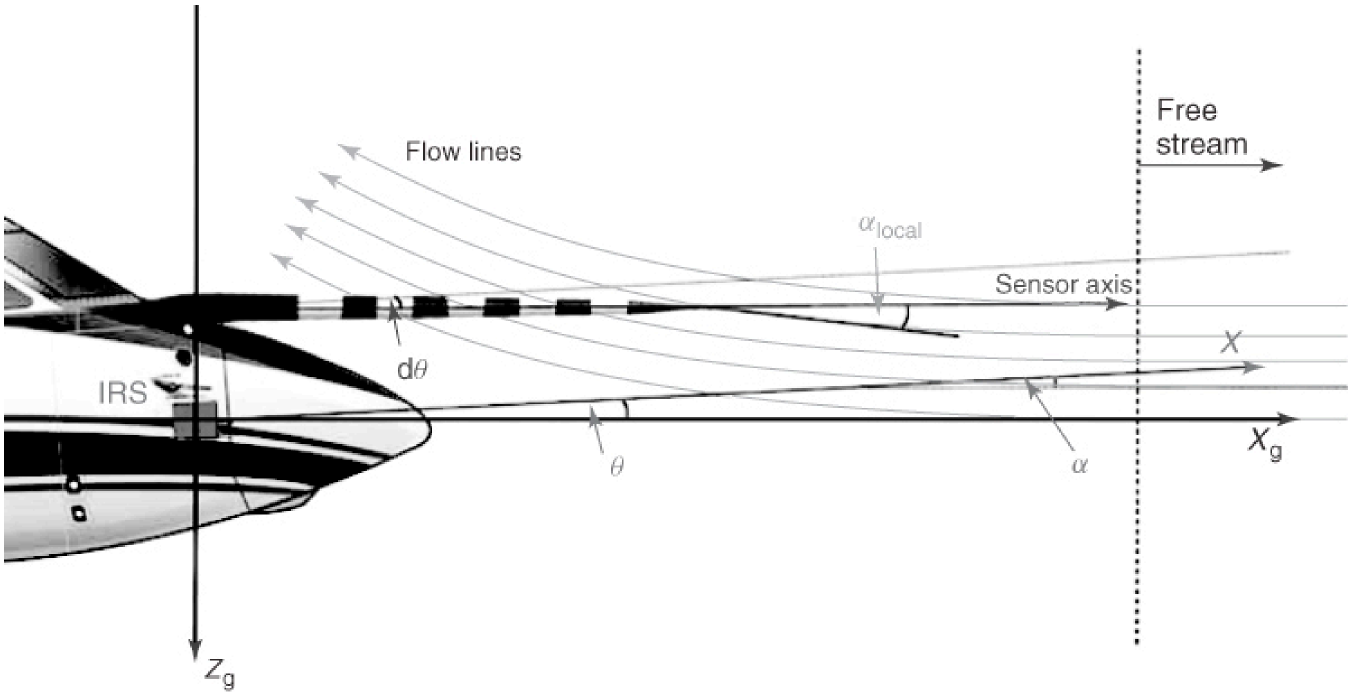

This means that the measurement of α and β require a detailed characterization of the airflow ahead of the aircraft and a precise knowledge about the position and orientation of IRS and the gust probe relative to each other. The aircraft-induced vertical deflection of the flow lines is also known as upwash. When the gust probe is not installed on the aircraft nose or a centered nose boom (e.g., a wing-mounted boom), there will be a lateral deflection of the flow lines, which is called *sidewash*.

2.7.2 Errors and Flow Distortion

2.7.2.1 Parameterization Errors

The calculation of atmospheric parameters such as pressure, temperature, or flow angles from an initial measurement always involves correction terms or specific sensitivity coefficients. These terms account for aerodynamic effects or certain

sensor properties and they usually depend on flight parameters such as the Mach number and the flow angle. While some of them are provided by the manufacturer of the respective sensor, many others are specific to the aircraft and the sensor configuration. They have to be determined by the aircraft operator using in-flight calibration procedures or airflow analysis (Lenschow and Spyers–Duran, 1989; Boegel and Baumann, 1991; Crawford, Dobosy, and Dumas, 1996; Kalogiros and Wang, 2002).

2.7.2.2 Measurement Errors

A proper calibration must cover the whole logical chain between the sensor and the data acquisition. Depending on the aircraft being used, the required data range can be significant: −70 °C, 200 hPa, and stratospheric humidity require sophisticated calibration equipment. The impact of environmental conditions on a sensor can be significant and is hard to detect during flight. An example is the sensitivity of a pressure sensor to low temperatures or accelerations. A very special sensor is the IRS, one must investigate the instrument during flight in order to learn about its characteristics. In some cases, GPS data and sophisticated filter methods are used to improve the accuracy of aircraft position or velocity data (Lenschow and Spyers-Duran, 1989; Khelif, Burns, and Friehe, 1999).

2.7.2.3 Timing Errors

The processing of wind speed involves many different data sources each having its own characteristic temporal behavior, that is, different response time constants or delays, caused by physical properties of the sensing element or electronic (processing) delays. For humidity and temperature, these response times are not constant but depend on parameters such as the aircraft speed and static pressure. It is immediately clear that the wind calculation will have possibly large errors if one uses data sources that are not exactly synchronized (Lenschow and Spyers-Duran, 1989). Any time shift between the different time series will lead to artificial wind signals because the contributions caused by aircraft motion will not completely cancel each other out. In-flight calibration techniques are necessary to identify these delays, which have to be applied during data processing (Lenschow and Spyers-Duran, 1989; Boegel and Baumann, 1991).

2.7.2.4 Errors due to Incorrect Sensor Configuration

The wind signal can be degraded by vibrations of a "soft" nose boom and by long pressure lines between the gust probe and the pressure sensor (Whitmore 1990). Especially on large aircraft, the fuselage can no longer be seen as rigid and a large distance between flow angle sensor and IRS will cause errors due to fuselage bending. Misalignment of sensors is another problem that concerns the IRS and the nose boom (i.e., flow sensor) orientation.

2.7.3 In-Flight Calibration

The calibration of wind sensing systems is a complex task that begins with the ground calibration of each instrument in the system (pressure, temperature, humidity), includes the characterization of the probe in wind tunnel, and ends with in-flight calibration of the whole system. Two different ways of performing in-flight calibration are common: the Lenschow and Rodi maneuvers. More advanced techniques such as measurement of divergence (Lenschow, Savic–Jovcic, and Stevens, 2007) can provide a very accurate calibration/verification of the horizontal wind measuring system. The in-flight calibration can be found in Section A.1.3, given in the Supplementary Online Material provided on the publisher's web site.

2.8 Small-Scale Turbulence

Turbulence in atmospheric flows plays a dominant role for many processes such as mixing, turbulent transport, and collisions of particles (Wyngaard, 2010). In principle, the contributing scales range from the largest scale L that has the dimension of the considered phenomenon itself (e.g., the boundary layer height for convective plumes or the cloud diameter for cloud turbulence) down to the dissipation scale, also called the *Kolmogorov microscale* η given by

$$\eta = \left(\frac{\nu^3}{\bar{\varepsilon}}\right)^{1/4} \tag{2.39}$$

with the air viscosity $\nu \approx 1.5 \times 10^{-5} \mathrm{m}^2\ \mathrm{s}^{-1}$ and the mean turbulence energy dissipation rate per unit mass of

$$\overline{\varepsilon} \sim \frac{u_{\mathrm{rms}}^3}{L} \tag{2.40}$$

where u_{rms} is the root-mean-square value of the flow velocity. For typical atmospheric conditions, η is on the order of millimeters; that is, atmospheric turbulence spans a huge range of spatial scales resulting in high Reynolds' number:

$$\mathrm{Re} = \frac{L \cdot u_{\mathrm{rms}}}{\nu} \sim \left(\frac{L}{\eta}\right)^{4/3} \tag{2.41}$$

Therefore, the atmosphere provides a natural laboratory for high Reynolds' number turbulence, characterized by strong small-scale intermittency. This makes small-scale turbulence measurement in the atmosphere also appealing for fundamental turbulence research.

This section focuses on sensors and devices suitable for airborne small-scale turbulence measurements. With some arbitrariness, the "small scales" are defined as scales within and below the inertial range, typically below the order of tens of meters or so where standard aircraft instrumentation has its limitation. An introduction of a few basic concepts of sampling requirements can be found in Section A.2, given in the Supplementary Online Material provided on the publisher's web site.

2.8.1 Hot-Wire/Hot-Film Probes for High-Resolution Flow Measurements

If flow measurements with a resolution down to the dissipation scale are required, there is no alternative to hot-wire anemometry. Note that if a more robust sensor is required for airborne applications, thin hot-film probes might be used instead of the fragile thin wires with a slight reduction of temporal resolution. The basic principle of hot-wire anemometry is the forced convection of a heated sensing wire in a fluid. "Forced" convection means that the bulk relative velocity between sensor and fluid is due to external forces, whereas "natural" convection is due to buoyancy. The heat transfer power (measured in Watts) can be described as

$$W = U \cdot A \cdot (T_{\mathrm{sen}} - T_{\mathrm{f}}) \tag{2.42}$$

with the sensor temperature T_{sen}, the fluid temperature T_{f} (all temperatures in K), the surface area of the sensor A, and the convective heat transfer coefficient U (in units of $\mathrm{W\ m^{-2}\ K^{-1}}$). Here, the conduction heat transfer between the heated portion of the sensor and its support is ignored for simplicity.

The dimensionless Nusselt number is defined as

$$\mathrm{Nu} = \frac{L \cdot U}{\kappa} \tag{2.43}$$

where L is a typical dimension and κ is the thermal heat conductivity. The dependence of the dimensionless Nusselt number Nu on the convection heat transfer coefficient U is used to relate the heat transfer to the flow velocity u. For forced convection from a cylinder, the Nusselt number is semiempirically found as

$$\mathrm{Nu} \approx 0.24 + 0.56 \cdot \mathrm{Re}^{0.5} \tag{2.44}$$

where $\mathrm{Re} = u \cdot d/\nu$ is the Reynolds number of a flow around a wire with diameter d and ν is the fluid viscosity, often referred to as *King's law* (King, 1914). This finally results in

$$U = \frac{0.24\,\kappa}{d} + 0.56\,\kappa \cdot \sqrt{\frac{u \cdot d}{\nu}} = a + b \cdot \sqrt{u} \tag{2.45}$$

Thus, the convection heat transfer coefficient U depends on the geometrical sensor, physical fluid properties, and the flow velocity u.

The most common type of hot-wire anemometer is the constant temperature anemometer (CTA). Here, the sensor temperature T_{sen} and, therefore, the resistance of the sensing wire (R_{sen}) are maintained at a constant value. With the heating current I, we find that for steady-state conditions,

2.46 $$W = I^2 \cdot R_{\text{sen}} = U \cdot A \cdot (T_{\text{sen}} - T_{\text{f}})$$

If the flow velocity u increases, U will increase and the system has to increase I through the sensor to restore equilibrium. Since R_{sen} is constant, the voltage drop $E_{\text{out}} = I \cdot R_{\text{sen}}$ over the sensor increases with current, thus giving a voltage signal proportional to $u^{1/4}$.

The main advantage of a CTA is its high bandwidth of up to 100 kHz (or higher) over a huge range of flow velocities. With multisensor probes, the two-dimensional (2D) or 3D velocity vector can also be measured. Sensor calibration can be performed with the help of special pressure nozzles in a free jet created by compressed air up to Mach 1. The disadvantage of hot wires, especially on aircraft, is their fragility and that each sensor has to be carefully calibrated individually, including its supports, connectors, and cables. Alternatively, the sensor can be calibrated by comparing with a standard anemometer (e.g., gust probe) as in-flight calibration or postprocessing. The hot-wire signal is highly nonlinear in u, and calibration depends on the temperature difference between the sensor and the environment. More sophisticated probes are temperature compensated. The influence of natural convection around the sensing wire can be neglected for airborne measurements because of the high TAS. Although robust hot-film probes are available for high TAS (with some degradation of the bandwidth), only a few airborne measurements are reported (Sheih, Tennekes, and Lumley, 1971; Merceret, 1976a; Merceret, 1976b; Lenschow, Friehe, and Larue, 1978; Payne and Lumley, 1965). Most hazards to the wires are due to impacting aerosol particles (in particular, during takeoff and landing) or cloud droplets (Siebert, Lehmann, and Shaw, 2007; Siebert, Shaw, and Warhaft, 2010), and aircraft vibration. Electromagnetic noise can also be troublesome, but it can be minimized with shielded cables and by placing signal amplifiers and data recording devices as close to the sensors as possible.

A more detailed introduction of all aspects of hot-wire anemometry can be found in the works by Comte-Bellot (1976), Bruun (1995), and Goldstein (1996).

2.8.2 Laser Doppler Anemometers

Laser Doppler velocimetry (LDV) provides a measurement of the speed of particles in a flow, via heterodyne detection of Doppler-shifted light scattered by individual particles. The method has been refined and widely adopted for the study of engineering flows, and detailed reviews are available (Adrian, 1996; Buchhave, George, and Lumley, 1979). The method has been further modified to enable determination of the diameter of spherical particles (Bachalo, 1980). It is relatively recent that LDV has become sufficiently robust to be commonly used for atmospheric measurements (Chuang 2008). For example, it has been used in the measurement of turbulence statistics in clouds where other methods can be troublesome due to the multiphase environment (Siebert 2006a). Because the method measures the speed of particles, rather than the flow itself, it can be of considerable use in studying dynamics of inertial particles in turbulence (Saw 2008).

The physical principle underlying LDV is the Doppler shifting of light scattered by particles such as cloud droplets or aerosol particles that are moving relative to a light source and detector. The Doppler shift in the detected radiation is exceedingly small in practical terms. Therefore, the measurement is made by mixing two slightly different Doppler-shifted signals from the same particle and measuring the resulting beat frequency. The difference in frequencies arises from the geometrical arrangement of the two crossing laser beams. An additional user-imposed frequency shift from a Bragg cell is sometimes imposed to minimize directional ambiguity. The beat frequency is proportional to the component of the particle velocity vector that lies in the plane of the crossing laser beams perpendicular to the optical axis; see Section A.3 (given in the Supplementary Online Material provided on the publisher's web site) for a derivation of the frequency dependence on particle motion and system geometry. Additional velocity components can be measured with more complex, multilaser, and detector systems. As a particle moves through the beam-crossing region, the measured signal has the form of a Gaussian envelope, as a result of the Gaussian laser beam profile modulating the Doppler beat frequency.

By its very nature, LDV is ideally suited for measurements in clouds. The very droplets that tend to disturb other high-resolution methods, such as hot-wire anemometry (Section 2.8.1), are the source of the signal. The ability of an LDV system to accurately sample a turbulent flow field in a cloud depends on its spatial resolution and its velocity resolution. The spatial resolution is determined by the cloud particle number density and the instrument sample cross section (modern sampling systems are designed such that sampling frequency is not a limiting factor). In practice, because of the nonuniform spatial sampling, the effective resolution can be degraded to as much as 10 times the average distance between sampled cloud particles. The velocity resolution must be sufficiently fine to capture typical velocity fluctuations corresponding to a desired spatial scale r. For a turbulent flow with kinetic energy dissipation rate ε, the magnitude of the velocity fluctuations can be estimated from

2.47 $v_r = (\varepsilon \cdot r)^{1/3}$

The velocity resolution scales with the resolution with which the Doppler beat frequency can be measured. Ultimately, this depends on instrument parameters such as signal-to-noise ratio (SNR), sampling frequency, and sample volume size via the Cramer–Rao error estimate (Chuang 2008). Finally, it is again emphasized that particle, not fluid, speeds are measured. If the fluid speed is desired then a further source of error is the inability of large cloud particles to follow high-frequency velocity fluctuations. Typical cloud droplets of diameters up to ~30 μm can be safely approximated as flow tracers for the moderate energy dissipation rates of most clouds and for the purposes of estimates of average turbulence properties. Details on the response of cloud droplets to turbulent fluctuations are given in Section 4 of the work by Chuang (2008).

An example of a turbulent velocity spectrum from a cumulus cloud is shown in Figure 2.16. The solid curve is for data obtained from an LDV instrument (Chuang 2008), and the dashed curve is for data obtained simultaneously from a sonic anemometer. The measurements were made aboard the Airborne Cloud Turbulence Observation System (ACTOS) deployed via a helicopter (Siebert 2006a). The agreement between the two instruments is reasonable throughout the resolvable subset of the inertial range. Furthermore, both power spectra match, at least to within the sampling uncertainty, the expected − 5/3 power law dependence (exemplified by the dotted–dashed line) for the energy spectrum of the longitudinal velocity component within the inertial range. The energy spectra are plotted up to a spatial resolution of 20 cm (spatial frequency, 5 m^{-1}), which is approximately the limit of the sample-and-hold method used for the selected segment of LDV data, based on the average cloud droplet arrival frequency, as well as the spatial resolution of the sonic anemometer. The slight flattening of the LDV power spectrum at high frequencies is characteristic of the sample-and-hold method.

Figure 2.16 Turbulent velocity energy spectrum measured with an LDV system (solid) and a sonic anemometer (dashed); a line with a slope of − 5/3 is included for reference (dashed–dotted). (Source: Adapted from Figure 12 in Chuang (2008).)

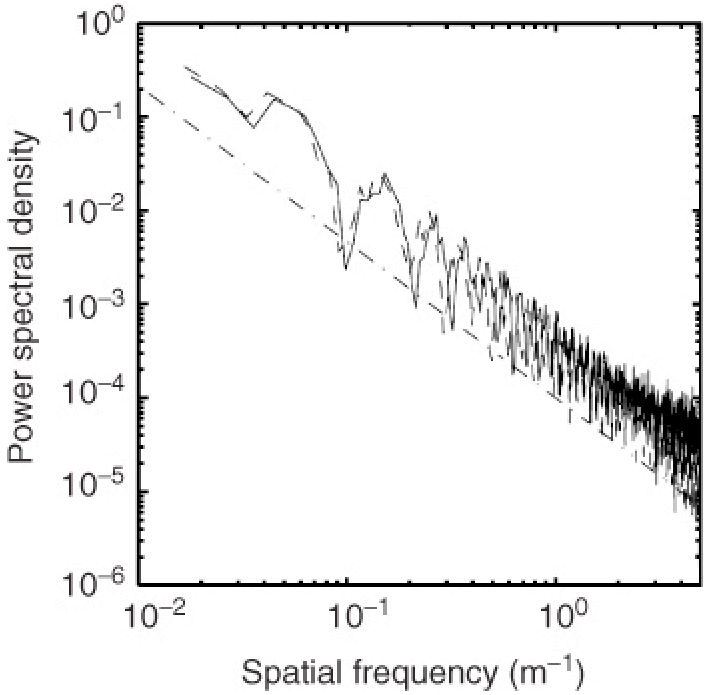

The focus here has been on Doppler measurements from light scattered by single particles (e.g., cloud droplets) at spatial and temporal resolution suitable for turbulence characterization. The essential elements of LDV have also been applied in a variety of systems, however. Doppler LIDARs typically measure light scattered from aerosol particles contained in a relatively large volume of air using a similar heterodyne detection method as LDV, for example, see review by Huffaker and Hardesty (1996). Furthermore, LIDAR systems operate with time (range) gates. Therefore, they provide velocity information over a region of space rather than in a single measurement volume. LIDAR-type laser Doppler techniques have been developed for airborne measurements of airspeed as well, and in principle, they offer several advantages over traditional measurement methods such as differential pressure. For example, the measurement volume can be located upwind of the disturbance generated by the moving aircraft and systems can be configured to offer spatial information

such as vertical wind shear. The system described by Keeler (1987) provided turbulence spectra up to ~10 Hz, allowing the large scales of the turbulence inertial subrange to be observed. A new system known as the *Laser Air Motion Sensor* developed at the NCAR (Spuler 2011) provides an absolute measurement of airspeed independent of flight maneuvers and atmospheric conditions and is being extended to include a single forward-pointing beam plus three 30° off-axis beams in a single wing-pod canister to allow measurement of the full wind vector.

2.8.3 Ultrasonic Anemometers/Thermometers

Ultrasonic anemometers/thermometers (hereafter called *sonics*) are standard devices for tower-based atmospheric boundary layer studies and turbulent flux measurements (Section 2.9). Even though such instruments are not widely used on aircraft, they have a few advantages, making them attractive for at least slow-flying aircraft and helicopter-borne applications at low TAS.

The basic principle of a simplified 1D sonic is transit time measurements of two subsequent sound pulses traveling with and against the wind component along two transducers T1 and T2, which are separated by a distance L. The first sound pulse is sent from T1 to T2 with pulse velocity $u_1 = c + U$ (where c is the speed of sound), and the second pulse is immediately sent back with a velocity $u_2 = c - U$ after the first pulse is received by transducer T2. The measured transit times t_1 and t_2 are $t_1 = L/(c + U)$*and* $t_2 = L/(c - U)$, and a combination of both equations yields

$$U = \frac{L}{2} \cdot \left(\frac{1}{t_1} - \frac{1}{t_2} \right) \tag{2.48}$$

and for the speed of sound,

$$c = \frac{L}{2} \cdot \left(\frac{1}{t_1} + \frac{1}{t_2} \right) \tag{2.49}$$

Note that in principle, the measurement of U depends only on the constant distance L and the two measured transit times but is independent of c, and the measurement of c is independent of U.

Under adiabatic conditions, c is given by

$$c = \sqrt{\gamma \cdot R_{\mathrm{dry}} \cdot T_{\mathrm{vir}}} \tag{2.50}$$

where $\gamma = c_p/c_v = 1.4$ is the adiabatic exponent (c_p and c_v are the heat capacities of dry air for constant pressure and constant volume, respectively), $R_{\mathrm{dry}} = 287\ \mathrm{J\ kg^{-1}\ K^{-1}}$ is the gas constant for dry air, and:

$$T_{\mathrm{vir}} = T \cdot \left(1 + 0.38\, \frac{p_w}{p} \right) \tag{2.51}$$

is the virtual temperature, with actual temperature T, air pressure p, and water vapor pressure p_w. With the same shot, the wind velocity component and the virtual temperature can be measured within the same volume, making this device quite attractive (Section 2.5.6). It is straightforward to design a configuration of three transducer pairs to measure the three-component wind vector. Typical resolution is about 1 cm s^{-1} for the velocity components and 10 mK for temperature measurements.

A few general design issues have to be considered. The ratio of the diameter of the transducer d and the distance L has to be small ($d/L \ll 0.1$ with L typically ~ 0.1 m) to keep transducer shadowing effects in an acceptable limit (Wyngaard and Zhang, 1985). The effect of line averaging over the path L is discussed by Kaimal, Wyngaard, and Haugen (1968).

Usually, standard ultrasonic anemometers used for ground-based studies cannot be applied directly to fast-flying aircraft without serious modifications of the framework and electronics. The maximum wind speed (approximate TAS on an aircraft) that can be measured with a sonic is limited to about 50 m s^{-1}, and the framework is usually not stiff enough to avoid vibrations (Siebert and Muschinski, 2001). However, a few special developments of sonics for aircraft and helicopter are in use, and TAS up to 100 m s^{-1} has been reported (Cruette 2000; Avissar 2009).

2.8.4 Measurements of Atmospheric Temperature Fluctuations with Resistance Wires

This section focuses on measurements of small-scale temperature fluctuations in turbulent atmosphere and clouds. Further description of airborne temperature measurements can be found in Section 2.5.

Generally, temperature readings from aircraft are strongly affected by temperature fluctuations due to dynamic pressure variations (depending on TAS and attitude angles of the aircraft), the effects of heat transport/thermal inertia of sensor supports and housings, and even the effects of viscous heating. Altogether these effects introduce bias and noise (in the case of unsteady flow around the sensor) and limit effective time constants to ~ 10^{-1} s (Friehe and Khelif, 1992; Mayer 2009). All these effects make measurement of small-scale temperature fluctuations difficult, especially in clouds and rain where wetting may cause problems (Lawson and Cooper, 1990; Sinkevich and Lawson, 2005).

The only sensors of resolution capable to detect small-scale temperature fluctuations from the aircraft described so far are fine resistive wires (2.5 μm diameter) with minimum shielding mounted on a vane that adjusts to the local flow. These ultrafast thermometers, UFTs, (Haman 1997, 2001) are developed on the basis of similar or even finer unshielded sensors used in laboratory turbulence research. Specific airborne requirements mean that even recent versions of UFTs are of limited applicability. They are unstable over long times, require laborious and frequent replacements of sensing elements, and have to be accompanied by a stable, calibrated, slow-response thermometer as a reference. Nevertheless, they provide high-resolution information not available with other techniques and are well suited for in-cloud measurements (Haman and Malinowski,1996; Siebert 2006a; Haman 2007).

The Prandtl number of air (the ratio of momentum and thermal diffusivities) is Pr ≈ 0.72. This means that smallest scales of temperature fluctuations η_t in turbulent airflow are close to the Kolmogorov microscale η:

$$\eta_t = \eta \cdot \mathrm{Pr}^{-3/4} \approx 1.28\,\eta \tag{2.52}$$

Assuming 100 m s^{-1} as a typical TAS of the aircraft and η on the order of 10^{-3} m, a required response time of the sensor resolving turbulent temperature fluctuations should be ~ 10^{-5} s with the corresponding size of the temperature sensor of ~η_t an order of magnitude less than the capabilities of UFT estimated from a heat balance equation (Haman 1997):

$$\frac{\mathrm{d}T_{\mathrm{sen}}}{\mathrm{d}t} = \frac{(T_{\mathrm{sen}} - T_{\mathrm{a}})}{\tau} \tag{2.53}$$

where T_{sen} is the temperature of the sensor; T_{a}, temperature of the air; and τ, the time constant. Assuming that the resistive wire is long (length-to-diameter ratio, ≥1000), τ can be estimated as

$$\tau = \frac{c_{\mathrm{sen}} \cdot d^2 \cdot \rho_{\mathrm{sen}}}{4\kappa \cdot \mathrm{Nu}} \tag{2.54}$$

where c_{sen} and ρ_{sen} are, respectively, the specific heat and density of the sensor material and d is the diameter of the cylinder (Nu is defined in Section 2.8.1). For a UFT sensing element consisting of a platinum-coated tungsten wire (length/diameter ratio, ≈2000) in the range of TAS of 25–100 m s^{-1} and viscosities of (1.46 – 2.03) × 10^{-5} m^2 s^{-1} gives τ = (0.71 – 1.37) · 10^{-4} s. This is slightly less than the experimentally measured response of UFT wire (1.68 ± 0.17 × 10^{-4} s at 40 ms^{-1}).

Figure 2.17 presents power spectral density of temperature fluctuations demonstrating the performance of UFTs. In Figure 2.17b (data recorded in turbulence of high-temperature contrasts), power spectral density follows −5/3 power law at a wide range of frequencies of 1–1000 Hz (wavelengths of 55 m–5.5 cm). In calm thermally homogeneous air (Figure 2.17a), power spectral density shows only very weak natural variance of temperature. In both panels, a peak at 90 Hz due to acoustic waves from the propellers can been seen, with the second harmonic obscured by natural temperature fluctuations in Figure 2.17b. Above ≈2 kHz, temperature fluctuations in vortices shedding from the protecting rod dominate. Amplitude/frequency of these vortices depends on TAS, and details of these effects were investigated experimentally by Haman (2001) and numerically by Rosa (2005). Vortex shedding limits the effective resolution of the UFT sensor down to ≈ 1 kHz cutoff frequency as illustrated by Kumala (2010). Temperature fluctuations at distances less than ≈ 5 cm are not properly resolved with UFT.

Figure 2.17 Power spectral density of temperature fluctuations close to the top of a stratocumulus cloud recorded by a UFT thermometer at TAS of 55 m s^{-1} (a) above clouds in calm air with no significant temperature fluctuations, (b) in the topmost part of a stratocumulus cloud undergoing mixing with dry environment.

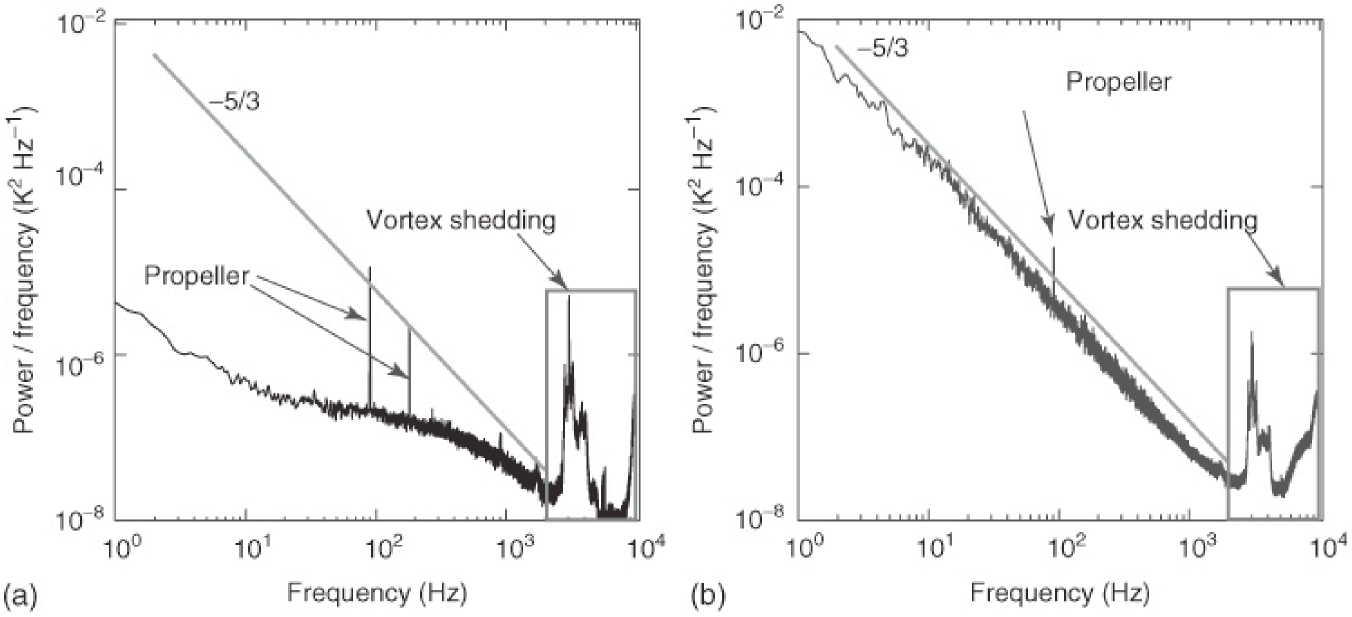

The relatively high-frequency response of the UFT creates many technical problems. Usually research aircraft are not equipped to record signals with sampling rates of 2×10^4 samples per second or more, and hence, special data acquisition systems are necessary. The sensor (bare wire) acts as an antenna and is sensitive to electromagnetic noise from radio, RADAR, and avionics. All these effects limit our abilities to measure small-scale processes in the atmosphere.

2.8.5 Calibration of Fast-Response Sensors

Many turbulence sensors are characterized by a high-frequency response with high sensitivity but low absolute accuracy and/or long-time drift. Such behavior is typical for fine-wire sensors, which have to be individually calibrated for each sensor element. This calibration can be performed in different ways, the most common procedures are (i) complementary filtering (e.g., Kálmán filters) or, more simply, (ii) calibration against other more accurate sensors by applying a regression.

Complementary filters perform low-pass filtering to a data set $s(t)$ measured by a highly accurate but slowly responding sensor, and high-pass filtering to a data set $f(t)$ measured by a fast sensor with poor long-term accuracy. Both filtered time series are then merged resulting in a highly accurate signal $n(t)$ with high temporal resolution. Such filters can be applied in real time (e.g., Kálmán filter, often used for navigation) or after the measurement as postprocessing. Two simple and fast methods for postprocessing are described in the following. For both methods, if the time series were not sampled at the same frequency, the slower one has to be interpolated before applying the filter.

The first method is based on Fourier transformations. Both time series $s(t)$ and $f(t)$ are Fourier transformed to complex series $\tilde{s}(\nu)$ and $\tilde{f}(\nu)$ (with frequency ν). After definition of a certain cutoff or merging frequency ν_c, all elements of $\tilde{s}(\nu)$ with $\nu > \nu_c$ and all elements of $\tilde{f}(\nu)$ with $\nu < \nu_c$ have to be removed. Then the two complex Fourier series are merged to a new complex Fourier series:

$$\tilde{g}(\nu) = [\tilde{s}(\nu_{min}) \ldots \tilde{s}(\nu_c), \tilde{f}(\nu_c) \ldots \tilde{f}(\nu_{max})] \quad \textbf{2.55}$$

which is finally transformed back to a new time series $g(t)$ using the inverse Fourier transformation. While this method is fast and easy, the two numerical Fourier transformations of finite data sets cause unwanted modification of the measured data due to imperfect data window functions (e.g., Hanning). Also, Fourier transformation is not very suited to time series of intermittent and nonperiodic signals (e.g., turbulence).

An alternative to the Fourier method is a filter in time like the Savitzky–Golay filter (Savitzky and Golay, 1964) that acts similar to a low-pass filter. It replaces each data point $s(t_i) \equiv s_i$ by a linear combination $\hat{S}$ of itself and a number $(n + m + 1)$ of nearby neighbors:

$$\widehat{s_i} = \sum_{j=-n}^{m} c_j \cdot s_{i+j} \qquad 2.56$$

Using a symmetric window $(n = m)$ with constant weights $c_j = (2n + 1)^{-1}$, the filter equals a moving-average window. More sophisticated Savitzky–Golay filters define c_j as a polynomial to preserve features of the time series such as local maxima and minima that are usually flattened by moving averages. Then, Eq. (2.56) represents the convolution of time series s with c.

A symmetric filter window $(n = m)$ is still suitable for most measurements. The width of the window is usually a function of the cutoff frequency ν_c and the data sampling frequency ν_s, for example, $n = \nu_s/\nu_c$ floored to the nearest integer. The high-frequency part of time series $f(t)$ (see above) is obtained by subtracting the low-frequency part $\widehat{f}(t)$ (Eq. (2.56)) from the original time series $f(t)$. Finally, the new time series (high accuracy and high resolution) is obtained from

$$g(t) = \widehat{s}(t) + f(t) - \widehat{f}(t) \qquad 2.57$$

2.8.6 Summary, Gaps, and Emerging Technologies

Besides the design of the sensor itself, the biggest challenge of airborne turbulence measurements is likely the location of the sensor on the aircraft to keep the influence of flow distortions below an acceptable threshold or to quantify the influence to compensate for. On fixed-wing aircraft, nose booms or wing pods are preferred locations for high-resolution measurements (see examples in Figure 2.18). Such integrated systems have the further advantage of closely collocated measurements of the different parameters (wind vector, temperature, and humidity), which allows a more detailed interpretation of covariances and correlation of different parameters.

Figure 2.18 Integrated nose boom for aircraft use to measure the wind vector, temperature, and humidity of the DO 128–6 of the Technische Universitt Braunschweig. (Source: Reprinted with permission of TU Braunschweig.)

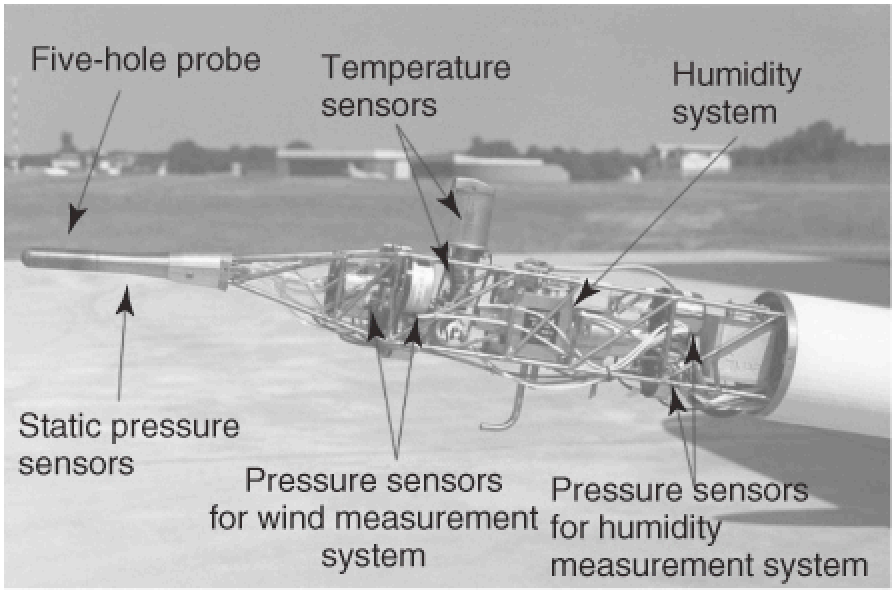

An alternative to fast-flying fixed-wing aircraft are integrated pods to be carried as external cargo by slow-flying helicopters. The influence of the rotor downwash can be overcome by an appropriate relation between tether length and minimum TAS. These setups are characterized by high flexibility and can be operated on board ships or in remote areas. Furthermore, due to the comparably low TAS, many technical limitations and sampling problems of fast-flying aircraft, such as adiabatic sensor heating or inlet problems, are significantly reduced. Another technical advantage of such compact

systems is the possibility of being maintained and calibrated in whole without any influence of the aircraft such as electromagnetic noise or similar hazards. At present, two such systems are in use and are shown as an example in Figure 2.19.

Figure 2.19 Two measurement payloads carried by helicopters as external cargo: (a) the "Airborne Cloud Turbulence Observation System ACTOS" and (b) the "Helipod." Both payloads contain various sensors to measure turbulent quantities. (Source: Courtesy of Holger Siebert and Jens Bange.)

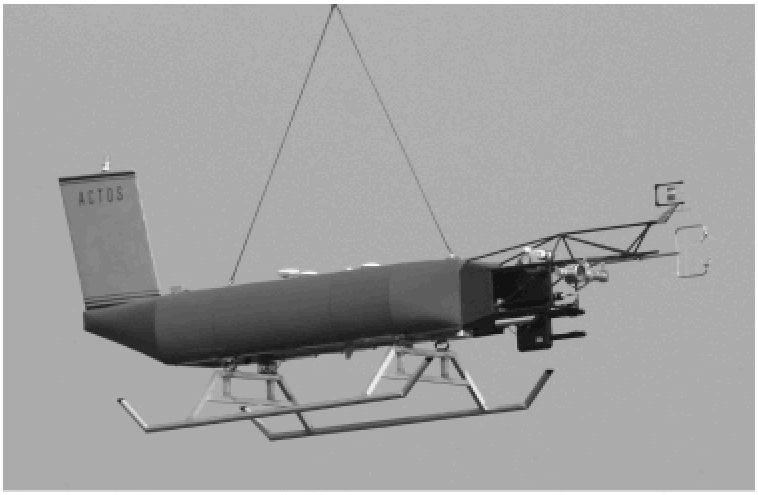

(a)

(b)

Another critical issue is the ability to perform high-resolution turbulence measurements in atmospheric clouds. The presence of droplets is critical for many turbulence probes. In particular, fine-wire sensors can be operated only under certain conditions (Siebert, Lehmann, and Shaw, 2007) or need special shielding to avoid droplet impaction (Section 2.8.4). Fast-response humidity measurements in cloudy environments are biased by possible evaporation of cloud droplet, which is difficult to quantify, and fast measurements of supersaturation with an absolute accuracy of a tenth of a percentage probably remain impossible for the near future.

2.9 Flux Measurements

2.9.1 Basics

Turbulent quantities in the Earth's atmosphere include the air pressure p, the air density ρ, the air temperature T, as well as the potential temperature θ, the mixing ratios m of the individual gases in the air (of special interests in meteorology are, e.g., water vapor, carbon dioxide, and ozone), and the wind vector $\boldsymbol{v} = (u,\ v,\ w)$. The calculation of the vertical turbulent fluxes of these quantities is the eddy covariance method (Montgomery, 1948). However, a covariance computed from a certain measured data set is only an estimator for the required ensemble-averaged covariance (Lenschow and Stankov, 1986; Crawford 1993). This estimator is defined via spatial averaging, assuming homogeneous turbulence. Since airborne measured data sets are usually time series, the spatial average is often substituted by a time average, assuming that (i)Taylor's hypothesis is fulfilled, (ii) the atmosphere is in a quasi-stationary state, and (iii) the aircraft's ground speed is constant. The last point is not true in real flight experiments, but then, no significant difference between fluxes calculated via spatial and temporal averaging has been found in experimental data (Crawford 1993). Also, nonevenly distributed spatial data makes Fourier analysis, for instance, more complicated. Therefore, time series and time averaging are used in the following.

To obtain the turbulent fluctuations $\phi'(t)$ of a measured time series $\phi(t)$, its mean value $\overline{\phi}$ has to be removed (the Reynolds decomposition). In practice, it is often recommended to remove a certain trend of the time series, especially for nonstationary situations (e.g., measurements around solar noon) and over heterogeneous terrain. This trend can be approximated by a linear regression, the second or third order of a polynomial regression, or the low-frequency modes of a Fourier series (i.e., removed by a high-pass filter). The detrending has to be carried out carefully because the resulting flux may be very sensitive to the definition of the trends and the mean values (Caramori 1994). The most commonly measured vertical turbulent fluxes in the lower atmosphere are

$$H = \rho \cdot c_p \cdot \overline{w' \cdot \theta'} \quad \text{Sensible heat flux} \tag{2.58}$$

$$LE = \rho \cdot L \cdot \overline{w' \cdot m'} \quad \text{Latent heat flux} \tag{2.59}$$

$$F_c = \overline{w' \cdot \rho_c'} \quad \text{CO}_2 \text{ flux} \tag{2.60}$$

$$\tau_x = -\rho \cdot \overline{w' \cdot u'} \quad \text{Horizontal momentum flux} \tag{2.61}$$

$$\tau_y = -\rho \cdot \overline{w' \cdot v'} \quad \text{Horizontal momentum flux} \tag{2.62}$$

where c_p = 1006 J kg^{-1} K^{-1} is the dry air isobaric specific heat, L = 2.5 × 10^6 J kg^{-1} K^{-1} is the latent heat of water vaporization, ρ is the mean air density at the measurement altitude, m is the mixing ratio of water vapor, and ρ_c is the CO_2 density.

2.9.2 Measurement Errors

In airborne atmospheric experiments, measurement errors may result from nonideal measurement equipment or disturbing effects that cannot be eliminated. These are, for instance, dynamic heating (Heinemann, 2002), oscillations of the instrument (e.g., organ pipe resonance in pressure tubes, nose boom oscillation, engine vibration, or pendulum oscillation; (Hauf (1984), Bange and Roth (1999)), or inexact static air pressure and geometric attitude measurement (Khelif, Burns, and Friehe, 1999). Additional sources of measurement errors are effects that limit the spectral range of the instrument, such as noise and slowly responding sensors (McCarthy, 1973; Isaac 2004), both of which mainly affect the high frequencies of the measured spectrum.

Many errors can be identified in a Fourier spectral analysis, for instance, noise in the power supply within a certain frequency range or sensor oscillation. If only one of the two turbulent quantities in each Eqs. (2.58)–(2.62) is affected by, for example, an oscillation, the corresponding flux error might be negligible because the oscillation and the turbulence are not correlated. This can be inspected in a Fourier cross-spectrum.

Broader effects such as high-frequency noise and comparison with the Kolmogorov hypothesis of locally isotropic turbulence within the inertial subrange can be analyzed using structure functions or spectra (i.e., the $k^{-5/3}$ or the $r^{2/3}$ law, respectively). The ability to measure small-scale turbulent fluctuations is limited by the sensor with the slowest response time when applying the eddy covariance method (Eqs. (2.58)–(2.62)). For example, if the minimum response time of the vertical wind measurement unit is 0.1 s but the temperature sensor response time is 1 s, only fluctuations slower than 1 Hz contribute to the measured sensible heat flux. The sensor response time should not be confused with the sampling rate of the system. A covariance can be measured by sampling at a rate much less than the time response of the slowest sensor if the measurement is made fast enough to resolve all the scales that contribute to the covariance. This is the basis for disjunct eddy sampling (Lenschow, Mann, and Kristensen, 1994; Rinne 2000; Rinne 2001; Karl 2002), which has been used to measure fluxes of trace species; the sample is collected quickly and the species subsequently measured by a slow-responding instrument. If the separation between samples is less than the integral scale (discussed in the next section), the random error of the covariance estimate is only slightly increased over that obtained from a higher sample rate measurement.

Measurement errors can also be caused by the experimental setup (i.e., the meteorological boundary condition and the flight strategy) and the data analysis method. For instance, mesoscale fluctuations usually mix with turbulent motions at the low-frequency transition of the measured spectrum. Under some meteorological conditions (especially under stable thermal stratification, see van den Kroonenberg (2008)) these can be separated from the turbulent flow during the data analysis. In a convective boundary layer (CBL), this is much more complicated (Howell and Mahrt, 1997). Here, convection is the main source of turbulence, and the transition between mesoscale structures and turbulent eddies may be smooth, so the mesoscale cannot be decoupled from the turbulent range.

This discussion reveals the variety of possible errors. In the framework of this book, it is impossible to give a universal recipe on how to avoid such errors for each and every instrument, scientific mission, and atmospheric condition.

2.9.3 Flux Sampling Errors

The following errors do not primarily involve sensor characteristics but are caused by the measurement strategy. In order to achieve a certain accuracy, a minimum flight distance has to be flown under quasi-stationary conditions, as the sampling error is a direct function of the sampling length (Lenschow and Stankov, 1986; Grossman, 1992; Lenschow, Mann, and Kristensen, 1994; Mann and Lenschow, 1994). Flight legs that are not large compared to the largest energy-transporting turbulent eddies cause systematic errors since they lead to a systematic underestimation- (or overestimation) of the turbulent fluxes (Grossman, 1984). In this regard, it should be noted that, for instance, a 10 km flight leg cannot be substituted by 10 legs of 1 km length because the coherence of the turbulent flow is destroyed by the fragmentation. The systematic error in an ensemble of 10 measurement flights that each underestimate the turbulent heat flux cannot be corrected by increased averaging.

A measured turbulent flux, that is, the vertical sensible heat flux H, is only an estimation of the ensemble-averaged vertical sensible heat flux H_E. The ensemble average is an average taken over many different flow realizations that have the same initial and boundary conditions. In the limit of the sample size going to infinity, the ensemble average approaches the ensemble mean and may be a function of both time and position. When the flow is steady and homogeneous, the ensemble, space, and time means are equal (under identical experimental conditions). The atmosphere is normally nonstationary and heterogeneous to some degree, in which case the concept of an ensemble average, and the following error estimates, are only approximations.

2.9.3.1 Systematic Flux Error

The absolute deviation of a certain flux measurement H from the (unknown) ensemble average is

$$\Delta H = |H - H_E| \tag{2.63}$$

This systematic flux error can be estimated by a simple expression (Lenschow, Mann, and Kristensen, 1994; Mann and Lenschow, 1994):

$$\Delta H \approx 2\frac{I_H}{P_m} \cdot |H| \tag{2.64}$$

as long as the averaging time P_m is large compared to the integral timescale I_H of the flux.

The integral scale I_ϕ is the outer scale or macroscale of a turbulent quantity ϕ (Rotta, 1972). The associated integral timescale can be interpreted as the correlation time, the persistence or memory of the turbulent flow (Kaimal and Finnigan, 1994). The transformation into the integral length scale is carried out by multiplication of the integral timescale by the aircraft's ground speed, assuming that Taylor's hypothesis of frozen turbulence is valid and that the ground speed variations are not too large (Crawford 1993). The length scale can then be interpreted as the typical size of the largest or most energy-transporting eddies.

The integral timescale of a measured quantity ϕ is defined by

$$I_\phi = \int_0^{\tau_1} \frac{\overline{\phi'(t+\tau)\cdot\phi'(t)}}{\overline{\phi'^2}}\,\mathrm{d}\tau = \int_0^{\tau_1} \frac{\mathrm{cov}_{\phi\phi}(\tau)}{var_\phi}\,\mathrm{d}\tau \tag{2.65}$$

In Eq. (2.65), ϕ represents turbulent quantities such as temperature, humidity, wind components, and combinations of these. Hence, an integral scale of a turbulent flux can be defined. For instance,

$$\phi(t) = \rho \cdot c_p \cdot w'(t) \cdot \theta'(t) \tag{2.66}$$

yields the integral timescale I_H of the vertical turbulent flux of sensible heat. In practice, I_H is calculated by integration from zero lag to the first crossing with zero at τ_1 (Lenschow and Stankov, 1986). In order to make quantitative estimates of statistical properties of a turbulence time series, the integral scale has to exist. Often it was reported that I_ϕ was difficult to calculate since the autocorrelation function – the integrand in Eq. (2.65) – behaved unpredictably (Mann and Lenschow, 1994; Lenschow, Mann, and Kristensen, 1994) or did not cross zero at reasonable lags (Lumley and Panofsky, 1964). Then an upper limit of integral scale (and thus an upper limit of the error) can be estimated by

$$I_H \le \frac{\rho \cdot c_p}{|H|} \cdot \sigma_w \cdot \sigma_\theta \cdot \sqrt{I_w \cdot I_\theta} \tag{2.67}$$

with the integral timescales I_θ and I_w of θ and w, respectively, and their standard deviations,

$$\sigma_\theta = \sqrt{\mathrm{Var}_\theta} \tag{2.68}$$

and

$$\sigma_w = \sqrt{\mathrm{Var}_w} \tag{2.69}$$

Combining Eq. (2.67) with Eq. (2.64), the upper limit of the systematic flux error is

$$\Delta H \le 2\rho \cdot c_p \cdot \sigma_w \cdot \sigma_\theta \cdot \frac{\sqrt{I_w \cdot I_\theta}}{P_m} \tag{2.70}$$

2.9.3.2 Random Flux Error

In general, different measurements of finite duration P_m under identical boundary conditions will lead to different fluxes and different deviations from the ensemble mean. The random flux error is defined as the averaged squared differences between the ensemble and the actually measured fluxes:

$$\sigma_H^2 = \overline{(H_E - H)^2} \tag{2.71}$$

thus σ_H can be interpreted as the standard deviation of the measured flux H. For any turbulent quantity ϕ, and for measurement (averaging) periods P_m much larger than the integral timescale I_ϕ, an estimate for the random error is given by the variance (Lumley and Panofsky, 1964; Lenschow and Stankov, 1986):

$$\sigma_\phi^2 = 2\frac{I_\phi}{P_m} \cdot \overline{\phi'^2} = 2\frac{I_\phi}{P_m} \cdot \left(\overline{\phi^2} - \overline{\phi}^2\right) \tag{2.72}$$

For instance, the random error of the vertical flux of sensible heat is then defined by (with $\phi = \rho \cdot c_p \cdot w' \cdot \theta'$)

$$\sigma_H^2 = 2\,(\rho \cdot c_p)^2 \cdot \frac{I_H}{P_m} \cdot \overline{(w' \cdot \theta')'^2}$$
$$= 2\,(\rho \cdot c_p)^2 \cdot \frac{I_H}{P_m} \cdot \left(\overline{w'^2 \cdot \theta'^2} - \overline{w' \cdot \theta'}^2\right) \quad \textbf{2.73}$$

The ratio of the systematic to the random flux error decreases slowly toward zero for large averaging time or measurement duration P_m:

$$\frac{\Delta H}{\sigma_H} \sim \frac{1}{\sqrt{P_m}} \quad \textbf{2.74}$$

In other words, an increasing measurement duration leads to a systematic error that becomes a decreasing fraction of the random error. Field campaigns with the Helipod and the Do 128 demonstrated that in a typical mid-European summer afternoon (heterogeneous terrain and a moderately CBL with some cumulus clouds), flight legs of 10 km length are sufficient to neglect the systematic flux error (Bange, Beyrich, and Engelbart, 2002). Furthermore, simultaneous flights of the Helipod and the Do 128 confirmed the dependence of σ_H on the flight distance. The applicability of this error analysis was also analyzed in numerical flight experiments (Schröter, Bange, and Raasch, 2000).

2.9.4 Area-Averaged Turbulent Flux

The turbulent fluxes of momentum and heat representative of an area or region can be achieved using area-covering flight patterns such as simple horizontal squares or horizontal grids (Bange 2006b). First, the individual fluxes are calculated by averaging continuous data for each straight and level flight section (leg). Then, for example, for a simple square and assuming homogeneity, all four legs at constant altitude z_f are averaged to obtain an estimator for the area-representative flux (in this example, the sensible heat flux):

$$H_{z_f} = \rho(z_f) \cdot c_p \cdot \frac{1}{4} \sum_{j=1}^{4} \langle w' \cdot \theta' \rangle_j \quad \textbf{2.75}$$

The random error of H measured on a square flight can be obtained from the Gaussian error reproduction calculated from the individual errors of the four flight legs:

$$\sigma_H = \frac{1}{4} \sqrt{\sum_{j=1}^{4} \sigma_{H_j}^2} \quad \textbf{2.76}$$

Of course, four samples give only a measure of the random error.

The total vertical flux of horizontal momentum is defined by combination of Eqs. (2.61) and (2.62) as

$$\tau_{xy} = \sqrt{\tau_x^2 + \tau_y^2}$$
$$= \rho(z_f) \cdot \sqrt{\overline{w' \cdot u'}^2 + \overline{w' \cdot v'}^2} \quad \textbf{2.77}$$

The corresponding random flux error is again calculated using the Gaussian error propagation (Bange, Beyrich, and Engelbart, 2002):

$$\sigma_{\tau_{xy}}^2 = \left(\frac{\partial \tau_{xy}}{\partial \tau_x} \cdot \sigma_{\tau_x}\right)^2 + \left(\frac{\partial \tau_{xy}}{\partial \tau_y} \cdot \sigma_{\tau_y}\right)^2$$
$$= \left(\frac{\tau_x}{\tau_{xy}} \cdot \sigma_{\tau_x}\right)^2 + \left(\frac{\tau_y}{\tau_{xy}} \cdot \sigma_{\tau_y}\right)^2 \quad \textbf{2.78}$$

For many applications the surface flux is of interest. Besides flying extremely low, there are also methods to extrapolate airborne measured fluxes to surface level from area-covering flight patterns (Bange 2006b). At first, it seems reasonable to perform area-representative flux measurements above the atmospheric boundary layer flux blending height (Wieringa, 1986; Cantrell, 1991; Mahrt, 2000; Mahrt, Vickers, and Sun, 2001) since there the influence of the individual surface

patches within a heterogeneous land surface vanish. But then this blending height can be poorly defined or quite high, up to the middle of the atmospheric boundary layer (Bange 2006a), where the fluxes are small or not definable and difficult to be extrapolated to the ground.

2.9.5 Preparation for Airborne Flux Measurement

Finally, this section provides a rough guide on how to prepare for airborne measurements of vertical turbulent fluxes. In order to measure turbulent fluxes of thermodynamic quantities and others, the corresponding sensors should be installed in front of disturbing aircraft elements such as wings and propulsion, ideally mounted on a nose boom. All sensors should be installed within a small volume in order to avoid significant phase shifting between the measurements. If there are significant longitudinal displacements of sensors, or time lags introduced by, for example, sampling ducts, the fluxes have to be corrected by shifting the time series of one variable relative to the other before calculating the flux.

The quantities to measure are ground speed vector (in the inertial coordinate system), altitude above ground and above mean sea level, the Euler angles and angle rates, TAS vector, static air pressure or air density, air temperature, humidity, and other scalars of interest. Of course, all sensors have to be calibrated before flight.

Sensors that have a short response time (that allow for fast sampling rate and thus a high temporal and spatial resolution) usually are not long-time stable and vice versa. To achieve high-resolution measurements that do not drift in time due to changing sensor physics (for instance, contamination of a very thin resistance thermometer), a second, slower but more stable, sensor can be used complementarily (Muschinski and Wode, 1998; van den Kroonenberg 2008).

Most sensors are only calibrated for small angles of attack, sideslip, and acceleration. Also the flow around the aircraft can become quite complicated and disturbed during flight maneuvers. Thus, turbulent fluxes should be measured during level flight sections that are straight (legs) or with only small turn rates (i.e., $< 0.3° \, s^{-1}$).

The legs should be as long as possible although nonstationarity of the atmosphere and heterogeneity of the experimental site have to be taken into account. With surface heterogeneity, flight tracks are often partitioned to provide more meaningful flux estimates and restore applicability of the random error estimates. This procedure limits the length of the flight track.